

# Multiple nodal superconducting phases and order-parameter evolution in pressurized $\text{UTe}_2$

Shuo Zou<sup>1\*</sup>, Fengrui Shi<sup>2\*</sup>, Zhuolun Qiu<sup>1\*</sup>, Jialong Zhang<sup>3</sup>, Yan Zhang<sup>2</sup>, Weilong Qiu<sup>2</sup>, Zhusuo Wang<sup>1</sup>, Hai Zeng<sup>1</sup>, Yinina Ma<sup>4</sup>, Zheyu Wu<sup>5</sup>, Andrej Cabala<sup>6</sup>, Michal Vališka<sup>6</sup>, Ning Li<sup>7</sup>, Zihan Yang<sup>2</sup>, Kaixin Ye<sup>2</sup>, Jiawen Zhang<sup>2</sup>, Yanan Zhang<sup>2</sup>, Kangjian Luo<sup>1</sup>, Binbin Zhang<sup>7</sup>, Alexander G. Eaton<sup>5</sup>, Chaofan Zhang<sup>7</sup>, Gang Li<sup>4</sup>, Jianlin Luo<sup>4</sup>, Wen Huang<sup>3†</sup>, Huiqiu Yuan<sup>2‡</sup>, Xin Lu<sup>2§</sup>, and Yongkang Luo<sup>1¶</sup>

<sup>1</sup> *Wuhan National High Magnetic Field Center and School of Physics, Huazhong University of Science and Technology, Wuhan 430074, China;*

<sup>2</sup> *Center for Correlated Matter and School of Physics, Zhejiang University, Hangzhou 310058, China;*

<sup>3</sup> *School of Physical Sciences, Great Bay University, Dongguan 523000, China;*

<sup>4</sup> *Beijing National Laboratory for Condensed Matter Physics, Institute of Physics, Chinese Academy of Sciences, Beijing 100190, China;*

<sup>5</sup> *Cavendish Laboratory, University of Cambridge, Cambridge CB3 0HE, United Kingdom;*

<sup>6</sup> *Charles University, Faculty of Mathematics and Physics, Department of Condensed Matter Physics, Prague 2 121 16, Czech Republic; and*

<sup>7</sup> *College of Advanced Interdisciplinary Studies and Nanhua Laser Laboratory, National University of Defense Technology, Changsha, Hunan 410073, China;*

(Dated: January 6, 2026)

---

\* These authors contribute equally to this work

† Electronic address: huangwen@gbu.edu.cn

‡ Electronic address: hqyuan@zju.edu.cn

§ Electronic address: xinluphy@zju.edu.cn

¶ Electronic address: mpzslyk@gmail.com

Spin-triplet superconductivity (SC) offers a unique avenue for realizing non-Abelian Majorana zero modes and thus the fault-tolerant topological quantum computation, and has attracted a broad audience for both fundamental research and potential applications. The recently discovered heavy-fermion spin-triplet superconductor candidate  $\text{UTe}_2$  has sparked great interest for its ultrahigh upper critical field and reentrant SC phases in the proximity to a field-polarized magnetic state. Despite extensive studies on the phase diagrams and competing orders induced by pressure and magnetic field, limited has been known about its SC order parameters and their evolution with these control parameters, largely due to the lack of appropriate symmetry-sensitive detections. Here, we report comprehensive point-contact spectroscopy measurements of pressurized  $\text{UTe}_2$  on the  $(0\ 0\ 1)$  surface. The observation of Andreev bound state strongly suggests the presence of a  $p_z$  component in the SC order parameters. Quantitative analysis based on an extended Blonder-Tinkham-Klapwijk model unveils  $B_{2u}$  or  $B_{3u}$  as the most likely representation for both ambient and pressurized  $\text{UTe}_2$ , and remarkably, the multiple SC phases can be distinguished by a single parameter  $\langle\Delta_z\rangle/\langle\Delta_{x(y)}\rangle$ , the relative weight between the  $p_z$ -wave and  $p_{x(y)}$ -wave pairings. These findings not only impose stringent constraints on the superconducting order parameter in  $\text{UTe}_2$ , but also provide key spectroscopic evidence for the existence of multiple SC phases tuned through pressure.

## INTRODUCTION

The classification of superconductors is fundamentally governed by the pairing symmetry of their order parameters. Unlike conventional superconductivity (SC) that arises from spin-singlet pairing (total spin  $S = 0$ , even parity), spin-triplet pairing ( $S = 1$ , odd parity) where electrons with parallel spins form Cooper pairs represents a major frontier in condensed matter physics. This distinction is profound because pairing symmetry not only dictates the microscopic mechanism of SC, but also constraints on their physical properties and hence application prospects. Crucially, spin-triplet superconductors may host Majorana zero modes (a kind of non-Abelian quasiparticles localized at topological defects or edges) that constitute a critical resource for fault-tolerant topological quantum computation [1–3]. A central but often unresolved challenge, however, is definitive identification of the order

parameter of spin-triplet superconductors (or candidates), many of which have been in long-standing controversy [4, 5]. In particular, analogous to the superfluid  $^3\text{He}$  [6, 7], the interplay between spin and orbital degrees of freedom can stabilize multiple superconducting phases under different conditions [8–11]. This renders the determination of SC order parameters even more challenging in that many routine experimental probes may lose their efficacy at the extremes of ultra-low temperature, high pressure ( $p$ ), or strong magnetic field ( $\mu_0\mathbf{H}$ ).

$\text{UTe}_2$ , standing out as a promising candidate of spin-triplet superconductor, has attracted tremendous recent attention [12–20]. Albeit with a relatively low critical transition temperature  $T_c$  ( $\approx 2$  K), it exhibits exotic superconducting properties, including upper critical fields far exceeding the Pauli limit along all principal axes [12], halo-structured reentrance of SC under ultra-high magnetic field [21–23], possible chirality and time-reversal symmetry breaking [16, 24, 25], pair density wave [26], strange metallicity [27, 28], etc. The pressure-induced phase diagram of  $\text{UTe}_2$  is intriguing, too. Three SC phases denoted by SC1-3 were reported under pressure [27, 29, 30]. Although the boundaries among these SC phases seem to be clear, whether these states are mutually independent, what their pairing symmetries are, and how their order parameters evolve with temperature and pressure remain fundamental open questions. Unfortunately, little is known about these issues due to the lack of symmetry-sensitive experiments under pressure to date [31].

A natural approach to addressing this challenge is to look into the gap structure and the associated in-gap Andreev bound state (ABS) on specific sample surface. As illustrated in Fig. 1, for an ABS to form at a surface with specular reflection condition, there must be a phase change between the incident and reflected quasiparticle wavefunctions to incur a destructive interference. This can be realized if one or all components of the gap function  $\Delta(\mathbf{k})$  changes sign upon going from  $\mathbf{k}$  to  $\mathbf{k}'$ . Such an ABS can be detected through point-contact spectroscopy (PCS) a technique well-suited for extreme conditions by measuring the differential conductance ( $G_{\text{NS}}$ ) with an appropriate geometric alignment between tunneling current  $\mathbf{I}$  and inter-nodal scattering wavevector  $\mathbf{q}_N$ , seeing Fig. 1(c-d). In this way, one assumes that the four possible spin-triplet pairings in  $\text{UTe}_2$  (cf. Table 1) can be distinguished, in part, because zero-energy ABS (ZABS) can show up on the (0 0 1) surface only in the nodal  $B_{2u}$  and  $B_{3u}$  irreducible representations (IRs) whose order parameters contain the  $k_z$  component;  $A_u$  may also exhibit in-gap ABS on this surface, however, due to the fully-gapped dispersion, these ABSs are off-center.

TABLE I: Possible pairing symmetries and the corresponding forms of the gap functions of UTe<sub>2</sub> classified according to the D<sub>2h</sub> point group [14, 32–34]. Note that we here ignore high-order terms beyond linear order of  $k_i$  ( $i = x, y, z$ ). Zero-energy Andreev bound state (ZABS) are expected on the (0 0 1) surface for  $B_{2u}$  or  $B_{3u}$  representation.

IR	Basis functions	UTe <sub>2</sub> D <sub>2h</sub>	Spin component	ZABS on (0 0 1)?
$A_u$	$\Delta_x k_x \hat{\mathbf{x}} + \Delta_y k_y \hat{\mathbf{y}} + \Delta_z k_z \hat{\mathbf{z}}$			No
$B_{1u}$	$\Delta_y k_y \hat{\mathbf{x}} + \Delta_x k_x \hat{\mathbf{y}}$		$\hat{\mathbf{z}}$	No
$B_{2u}$	$\Delta_z k_z \hat{\mathbf{x}} + \Delta_x k_x \hat{\mathbf{z}}$		$\hat{\mathbf{y}}$	Yes
$B_{3u}$	$\Delta_z k_z \hat{\mathbf{y}} + \Delta_y k_y \hat{\mathbf{z}}$		$\hat{\mathbf{x}}$	Yes

Herein, by systematic PCS investigations of UTe<sub>2</sub> under hydrostatic pressure, signatures of ZABS are observed on the (0 0 1) surface, unambiguously suggesting the presence of  $p_z$  component in the gap function. Fitting the results to an extended Blonder-Tinkham-Klapwijk (BTK) model, we further find that the SC pairings of UTe<sub>2</sub> most likely fall in the  $B_{2u}$  or  $B_{3u}$  representation, and the different SC phases under pressure can be distinguished by a single parameter  $\frac{\langle \Delta_z \rangle}{\langle \Delta_{x(y)} \rangle}$ , the relative weight between the  $p_z$ -wave and  $p_{x(y)}$ -wave pairings. Our study therefore offers an important clue to pinpoint the pairing symmetry in this compound, and also provides crucial spectroscopic evidence for the existence of multiple nodal SC phases therein.

## RESULTS

PCS is a powerful probe for the density of states and hence the gap structure of superconducting pairing [35–37]. At the interface between a normal metal (NM) and a superconductor, an electron incident from the NM is either specularly reflected or retro-reflected as a hole by creating a Cooper pair in the superconductor, the latter of which is the well-known Andreev reflection, cf. Fig. S4 in **Supplementary Information (SI)**. A schematic set-up for the PCS measurements of UTe<sub>2</sub> under hydrostatic pressure is illustrated in Fig. 2(a). To avoid Ag-Te reaction, we used Au epoxy instead. The contact points were located on the (0 0 1) surface, with the magnetic field applied along the **a**-axis. To verify the sample quality, the standard resistivity measurements were also conducted on the same sample, with electrical current along **a**. More details about experimental method can be found in the **Methods** section.

Figure S1(a) shows that the  $\rho(T)$  profile at ambient pressure is in good agreement with previously reported results for ultra-clean single crystals grown by the molten soft flux method [38, 39], exhibiting a high residual resistivity ratio (RRR) up to 410 and high superconducting transition temperatures  $T_c^0 = 2.1$  K and  $T_c^{\text{on}} = 2.6$  K. The low- $T$  part of  $\rho(T)$  under various pressures are displayed in Fig. S1(b-c), and a phase diagram is constructed by the false-color contour plot of  $\rho(p, T)$  in Fig. 2(b). At low pressure in the regime denoted SC1 ( $p < 0.3$  GPa),  $T_c$  is slightly suppressed with increasing pressure. Beyond this threshold, the resistive  $T_c$  turns up, and this yields a dome structure in the intermediate pressure regime  $0.3 < p \leq 1.4$  GPa; however, earlier bulk measurements including AC calorimetry and AC susceptibility measurements both revealed a dual-transition regime: a high-temperature phase (SC2) and a low-temperature phase (SC3) [27, 29, 30]. The boundaries among these SC phases are depicted by the dashed lines. For pressure above 1.4 GPa, two anomalies denoted by  $T_{\text{m}1}$  and  $T_{\text{m}2}$  appear just above  $T_c$ , characteristic of the magnetically ordered phases MO1 and MO2, respectively [see Fig. S1(c)].  $T_{\text{m}1}$  increases rapidly with pressure, while  $T_{\text{m}2}$  is weakly pressure dependent. Overall, the as-obtained phase diagram resembles those reported in the literature [27, 30, 31].

Turning now to the PCS results of UTe<sub>2</sub>. We start with the data at ambient pressure, as shown in Fig. 2(c). The normal-state spectrum is nearly flat. At 2.5 K, just below  $T_c^{\text{on}}$ , a slight hump appears in the differential conductance spectrum. As temperature decreases further, the hump stabilizes, forming a zero-bias conductance peak (ZBCP). Before relating such ZBCP to the feature of unconventional SC states [40], it is necessary to rule out other extrinsic origins. First, spurious ZBCP can be caused by heating effect in the thermal regime [42–44], in the regard that an increasing bias voltage causes the local current to exceed the critical current, and consequently  $G_{\text{NS}}$  decreases by forming a peak centering about  $V = 0$ . In this case, it is speculated that the amplitude of the peak shall be nearly temperature independent, while the width of the peak shall shrink rapidly with magnetic field. Here, we rule out this possibility because the shape of the peak degrades gradually with increasing  $T$ , and an application of a small field ( $< 2$  T) only weakly affects its width, as shown in Fig. S2(a). Second, magnetic scattering may also induce conductance peaks at zero bias [45, 46]. However, this is not relevant here because UTe<sub>2</sub> does not exhibit magnetic ordering at ambient pressure [12]. In addition, ZBCP are also observed in different samples (S2 and S3) with various contact sizes and resistances, seeing Fig. 2(e,f). The presence of stable

ZBCP in various samples strongly suggests the existence of zero-energy Andreev bound state, which further implies a high probability of nodes in the gap structure.

The results of PCS under pressure (measured with sample S1) are displayed in Fig. 3 and S3. At low pressure (e.g. 0.2 GPa), the spectrum remains largely similar to that at ambient pressure, cf. Fig. 3(a), indicating that the SC order parameter likely remains unchanged. Remarkable differences are seen above the first critical pressure  $\sim 0.3$  GPa. As shown in Fig. 3(b), at 0.6 GPa, besides the ZBCP that is present for low pressure, dips appear on both sides of the peak at low temperature. These dips become more pronounced upon cooling, accompanied by the appearance of additional humps at slightly higher bias. As we will further explain below, the appearance of these side dips suggests that these ZBCPs are intrinsic and associated with the formation of ZABS. Further increasing pressure to 1.0 GPa, the main features of the spectrum remain the same. However, a new minor peak appears inside the dip at low temperature, forming a double-dip structure, as can be seen in Fig. 3(c). Similar behavior can also be identified at 1.2 GPa [Fig. S3(c)]. Finally, at 1.4 GPa that is on the verge between SC and magnetically ordered phases, the central peak is substantially broadened with its top being nearly flat. Side-dip structure is also present at this pressure. To better visualize the evolution of PCS with pressure, we present contour plots of  $G_{\text{NS}}(V, T)$  in the bottom panels of Fig. 3.

## DISCUSSION

To elucidate the evolution of the PCS of  $\text{UTe}_2$  with applied pressure, we analyzed the data in two steps. First, we theoretically simulated the  $G_{\text{NS}}(V)$  in the framework of an extended BTK model, aiming to qualitatively screen out the potential pairing symmetry. After that, numerical fittings were conducted to extract the parameters such as SC gap  $\Delta$ , the Dynes broadening factor  $\Gamma$ , and the junction barrier strength  $Z$ . In accordance with the experimental setup, we consider a planar NM-SC junction whose interface is perpendicular to the crystallographic **c**-axis of  $\text{UTe}_2$ . For spin triplet SCs, the Andreev reflection is a more complex process as compared with that for conventional spin-singlet ones, in the sense that the reflection can take place through multiple channels,  $\Phi_1 = |\uparrow\uparrow\rangle$ ,  $\Phi_0 = (|\uparrow\downarrow\rangle + |\downarrow\uparrow\rangle)/\sqrt{2}$ , and  $\Phi_{-1} = |\downarrow\downarrow\rangle$ . A cartoon illustration is presented in Fig. S4.

In short, the differential conductance for PCS takes the following form,

$$G_{\text{NS}}(V, T) = G_0 \int_{-\infty}^{+\infty} \frac{\partial f(E - eV)}{\partial V} \sum_{\mathbf{k}_{\parallel}} \left\{ 1 + \frac{1}{2} \sum_{\alpha, \beta} [|a_{\alpha\beta}(E + i\Gamma)|^2 - |b_{\alpha\beta}(E + i\Gamma)|^2] \right\} dE, \quad (1)$$

where  $G_0$  represents the conductance of the junction in the normal state;  $a_{\alpha\beta}$  and  $b_{\alpha\beta}$  are functions of  $Z$ ,  $\Gamma$  and  $\Delta$ , standing for the Andreev reflection and normal reflection coefficients, respectively;  $\alpha$  and  $\beta$  denote the spin states. Details of the calculation are provided in the **SI**. We first only consider the representative cases with pure  $p_x$ ,  $p_y$  and  $p_z$ -wave gap functions. The numerical results are displayed in Fig. 4 and Fig. S5. In the limit of weak junction barrier (i.e. small  $Z$ ) of our planar junction, the conductance spectra of all three states are essentially the same. The differential conductance exhibits a peak whose value is obviously less than 2 regardless of the choice of other parameters in Fig. 4(b) (i.e.  $\Gamma$ ,  $T$  and  $\Delta$ ). This is similar to the behavior of other unconventional pairings, such as the  $d_{x^2-y^2}$ -wave pairing in the cases of various junction surface orientations [40, 41]. As  $Z$  increases, the conductance of the  $p_{x(y)}$ - and  $p_z$ -wave pairings behave in fundamentally different manners. For the  $p_{x(y)}$  pairing, the conductance peak diminishes with increasing  $Z$  and eventually forms a gapped spectrum at large  $Z$ . In contrast, the peak for the  $p_z$ -wave sharpens as  $Z$  increases, with a peak value that readily exceeds 2 at large  $Z$ . These pronounced ZBCPs originate from the zero-energy Andreev bound states at the junction interface (Fig. 1). Their formation is closely related to the sign change of the gap function  $\Delta_{\mathbf{k}}$  between the incident wavevector  $\mathbf{k} = (k_x, k_y, k_z)$  and the reflected quasiparticles, and thus allows for localized sub-gap states to develop. No such sign change occurs for pure  $p_x$  and  $p_y$  pairings, and hence no bound state formation therein. Notably, bound states can still form when  $p_z$  and  $p_{x(y)}$  pairings mix, as long as the sign-changing  $p_z$  component is finite. However, depending on the details of mixing, the sub-gap conductance may take on more complicated structures, as can be seen in e.g. Fig. S6. As a side effect, at large  $Z$  the presence of surface bound states tends to deplete the tunneling probability of the bulk continuum, which may then induce conductance side dips around the bias voltage  $V = \pm|\Delta|$ . These side dips, however, are not robust against pair-breaking scattering and may be smeared if the Dynes broadening  $\Gamma$  is large, seeing below.

We then consider pairings in various IRs as proposed for UTe<sub>2</sub> (see Table 1) [14, 32–34],

with representative results displayed in Fig. S6. Firstly, the conductance peak of a generic  $A_u$  pairing typically splits at any finite  $Z$  [Fig. S6(a)] - which is not observed in all of our samples measured [Fig. 2(d-f)]. Secondly, since the  $B_{1u}$  pairing lacks a component that changes sign upon taking  $k_z$  to  $-k_z$ , it cannot exhibit conductance side dips at any values of  $Z$  and  $\Gamma$ . Lastly, the  $B_{2u}$  and  $B_{3u}$  pairings are indistinguishable in this junction, and they both can qualitatively capture all main features of the experimental spectra in Figs. 2, 3 and S3.

With these in mind, we then compare and fit the experimental spectra mainly in the framework of  $B_{2u}$  (or  $B_{3u}$ ). The fittings for the ambient-pressure data for three samples are provided in Fig. 2(d-f), and the obtained parameters are listed in Tab. S1. Although the three samples exhibit distinct profiles of PCS, a common feature is that the peak values of the  $G_{\text{NS}}(V)$  are all less than 1.2, significantly lower than 2. This suggests that the  $p_{x(y)}$  pairing component plays a more dominant role than the  $p_z$  pairing. Albeit of the different values of  $Z$  and  $\Gamma$  obtained considering junction variation, all three samples yield a similar set of gap amplitudes  $\Delta_{x(y)}$  and  $\Delta_z$  with the ratio  $\Delta_z/\Delta_{x(y)} \approx 0.57(5)$ , which bolsters our confidence in these fittings. The temperature dependence of  $\Delta_{x(y)}$  and  $\Delta_z$  of sample S1 at ambient pressure is presented in Fig. S2(c); they both strongly violate the BCS's prediction, which again demonstrates the unconventional nature of SC in UTe<sub>2</sub>. It is worthwhile to mention here that an earlier PCS experiments on (0 0 1) and (0.4 0.6 0.7) facets at ambient condition suggested dominant- $p_y$  wave gap function [47]; a recent zero-energy surface state visualization by STM measurements on (0 -1 1) facet most favors  $B_{3u}$  IR[34]; their conclusions are qualitatively consistent with ours for ambient pressure.

Figure 5 summarizes the fitting in different regions of the phase diagram. Representative fitting curves are displayed in Figs. S7-8. For small pressure  $p = 0.2$  GPa, the results are quite similar to those at ambient pressure, and the  $p_{x(y)}$  pairing is still found to dominate with  $\Delta_z/\Delta_{x(y)} \approx 0.64(2)$ . For  $p = 0.6$  GPa, however, the amplitude of ZBCP increases to  $\sim 1.70$ , and most importantly, dips emerge symmetrically on the two sides of the central peak. These dips can only be reproduced by increasing the weight of  $p_z$  component, as shown in Fig. 5(c). The fitting yields  $\Delta_z/\Delta_{x(y)} \approx 1.03$ . The situation at 0.8 GPa is similar to that at 0.6 GPa, and the amplitude of the ZBCP is further increased to 2.08, cf Fig. 5(d). At even higher pressure, the standard fitting procedure can hardly capture the double-side-dip feature. The exact origin of the double side dips remains elusive. One may conjecture that

it arises from multiple gaps. An alternative possibility is due to pressure inhomogeneity, in the regard that the NM-SC junction may cover several SC domains with different gap parameters. For both cases, a linear superposition model to the total differential conductance ( $G_{\text{NS}}^{\text{total}}$ ) are applicable:

$$G_{\text{NS}}^{\text{total}}(V) = \sum_i w_i G_{\text{NS}}^i(V), \quad (2)$$

where  $G_{\text{NS}}^i(V)$  is the differential conductance for each channel, and  $w_i \in [0, 1]$  characterizes the fractional contribution. This model can fit the multi-dip behavior rather well as shown in Fig. 5(e). The ratio between the  $p_z$  and  $p_{x(y)}$  components is thus defined as

$$\frac{\langle \Delta_z \rangle}{\langle \Delta_{x(y)} \rangle} \equiv \frac{\sum_i w_i \Delta_z^i}{\sum_i w_i \Delta_{x(y)}^i}, \quad (3)$$

the pressure dependence of which at 0.3 K is presented in the inset of Fig. 5(a). It is clear that the weight of  $p_z$  wave pairing increases drastically going from the SC1 to SC3, and becomes dominant in the latter region. For  $p = 1.2$  GPa,  $\frac{\langle \Delta_z \rangle}{\langle \Delta_{x(y)} \rangle}$  reaches  $\sim 1.30$ .

To gain insight into the transition from SC2 to SC3, we analyzed the temperature dependent PCS at fixed  $p = 0.8$  GPa, as shown in Fig. 5(f). Remarkably, with decreasing temperature, the ratio  $\frac{\langle \Delta_z \rangle}{\langle \Delta_{x(y)} \rangle}$  first reduces, and then increases, with a minimum near 1.5 K. The results for  $p = 0.6$  and 1.2 GPa are supplemented in Fig. S9, where similar temperature dependence can be observed, with minima occurring at about 1.6 and 0.7 K, respectively. In contrast, this ratio is nearly temperature-independent at  $p = 0$  [Fig. S9(d)]. It is particularly interesting to note that the critical temperatures defined in association with the minimum of  $\frac{\langle \Delta_z \rangle}{\langle \Delta_{x(y)} \rangle}$  match well with the boundary between SC2-SC3 that was determined through AC calorimetry and AC magnetic susceptibility [27, 30], as shown in Fig. 5(a) (red open circles). The peculiar non-monotonic temperature dependence of  $\frac{\langle \Delta_z \rangle}{\langle \Delta_{x(y)} \rangle}$  is more likely indicative of an underlying phase transition between the SC2 and SC3 states than a mere crossover.

Additional remarks in order:

(1) Is  $A_u$  pairing possible for ambient-pressure UTe<sub>2</sub>? While  $B_{2u}$  (or  $B_{3u}$ ) model provides a compelling fit to our data, we should emphasize that our results cannot entirely exclude this possibility. In fact,  $A_u$  was supported by an ambient-pressure <sup>125</sup>Te NMR experiment where Knight shift - proportional to the spin susceptibility - was found to decrease below  $T_c$

for magnetic field along all principal axes [32], as well as thermal conductivity measurements that pointed to a fully gapped pairing state [48]. These works suggested that the SC order parameter  $\mathbf{d}$  may contain non-negligible components along all  $\hat{\mathbf{x}}$ ,  $\hat{\mathbf{y}}$  and  $\hat{\mathbf{z}}$  axes. However, we should also note that the change of Knight shift is rather anisotropic, meaning that a certain component of  $\mathbf{d}$  may be rather small. In this case,  $A_u$  representation may blur into a quasi- $B_{nu}$  representation, while PCS lacks the necessary resolution to tell them apart.

(2) What can the order parameters be for pressurized UTe<sub>2</sub>? From our PCS measurements, it is fairly likely that SC1-3 are mutually independent phases. First of all, SC3 differs from SC1 strikingly in that the former is  $p_z$ -dominant while the latter is more dominated by  $p_{x(y)}$  pairing. The peculiar temperature dependence of  $\frac{\langle \Delta_z \rangle}{\langle \Delta_{x(y)} \rangle}$  also hints a phase transition taking place at the boundary between SC2-SC3. It should be pointed out that an earlier <sup>125</sup>Te NMR experiment at 1.2 GPa [31] manifested that the Knight shift remains constant when it enters the SC2 phase from the normal state, but starts to drop at the boundary of SC2-SC3. This indicates that the  $\hat{\mathbf{y}}$ -component of  $\mathbf{d}$  should be vanishingly small for SC2 but considerable for SC3. In this sense, and also taking into account our PCS experiment,  $B_{2u}$  appears the most promising for SC2, while SC3 is probably of  $B_{3u}$  representation. If so, the transition at SC2-SC3 would be accompanied with a transform of order parameter from  $\{p_z, p_x\}$  to  $\{p_z, p_y\}$ . However, we must admit that before a more systematic PCS investigation is made on other surfaces of UTe<sub>2</sub>, it is premature to draw a precise conclusion.

In summary, we systematically investigated the pressure-evolution of point-contact spectroscopy in UTe<sub>2</sub>. Clear and reproducible ZBCP is observed on the (0 0 1) surface, and the profile of the ZBCP is strongly pressure dependent with pronounced side-dip structure appearing for pressures above 0.3 GPa, indicating a nodal character in the gap structure of the multiple SC phases in UTe<sub>2</sub>. Quantitative analysis based on an extended BTK model suggests  $B_{2u}$  (or  $B_{3u}$ ) as the most conceivable irreducible representation for both ambient and pressurized cases, with the ratio  $\frac{\langle \Delta_z \rangle}{\langle \Delta_{x(y)} \rangle}$  serving as a useful parameter to differentiate the SC1-3 phases. It is found that the weight of the  $p_z$ -wave component increases drastically from SC1 to SC3, and the SC2-SC3 transition may be across different irreducible representations, e.g.  $B_{2u}$  to  $B_{3u}$ . Our work not only provides spectroscopic evidence for the existence of multiple SC phases in pressurized UTe<sub>2</sub>, but also places critical constraints on its superconducting order parameter, thus collectively establishing UTe<sub>2</sub> as a prototypical system for studying intertwined electronic orders upon pressure tuning.

## METHODS

### Single crystals preparation and characterization

High-quality single crystals of  $\text{UTe}_2$  were grown by a molten soft flux method as described elsewhere [38, 39]. We employed a mixture of  $\text{NaCl}$  and  $\text{KCl}$  as a flux. High-purity U (99.999%), Te (99.9999%),  $\text{NaCl}$  (99.99%) and  $\text{KCl}$  (99.999%) were mixed in a molar ratio of 1:1.71:60:60. To prevent contamination or oxidation of the starting materials, the entire process was carried out in an Ar-filled glove box. The mixture was transferred into a carbon crucible and sealed in quartz tube which was then heated up to 473 K and dwelt for 12 hours. The temperature was then raised to 723 K in 24 hours, held at this temperature for an additional 24 hours, and subsequently increased to 1223 K at a rate of 0.35 K/min and maintained for another 24 hours. After that, the temperature was gradually reduced to 923 K at a rate of 0.03 K/min, kept stable for 24 hours, and finally cooled to room temperature over the next 24 hours. This controlled thermal profile ensured the synthesis of high-quality crystalline materials.

### Measurements under pressure

Electrical transport measurements of  $\text{UTe}_2$  (sample S1) were performed in an 8 T superconducting magnet system, using a  $^3\text{He}$  refrigerator (Oxford Instruments). Prior to junction fabrication, the surfaces of the sample were fine-polished to obtain a fresh crystallographic (0 0 1) plane. A soft point-contact junction was then prepared by depositing a minimal droplet of Au epoxy (54L-2210) to glue the gold wires onto the fresh surface. The small Au particles in the epoxy are solutes in the organic suspension, enabling the construction of a point contact with a small effective contact area. The Au epoxy was heated at 423 K for 30 minutes before the sample was transferred into a pressure cell. All these processes were conducted in an argon-filled glove box. A hybrid piston-clamp type cell was used to achieve quasi-hydrostatic pressures up to  $\sim 1.8$  GPa with Daphne 7373 oil serving as the pressure-transmitting medium. This rigorous sample preparation protocol preserves the intrinsic surface integrity of  $\text{UTe}_2$  and provides a stable electrical interface that is essential for the accurate probing of quasi-particle dynamics. To check the reproducibility of the results, two additional samples (S2 and S3) were measured at ambient pressure.

## Data availability

The authors declare that all source data supporting the findings of this study are available within the paper.

---

- [1] Alicea, J. New directions in the pursuit of Majorana fermions in solid state systems. *Pep. Rrog. Phys.* **75**, 076501 (2012).
- [2] Beenakker, C. W. J. Search for Majorana fermions in superconductors. *Annu. Rev. Condens. Phys.* **4**, 113-136 (2013).
- [3] Sato, M. & Ando, Y. Topological superconductors: a review. *Rep. Prog. Phys.* **80**, 076501 (2017).
- [4] Mackenzie, A. P. et al. Even odder after twenty-three years: the superconducting order parameter puzzle of  $\text{Sr}_2\text{RuO}_4$ . *npj Quantum Mater.* **2**, 40 (2017).
- [5] Pustogow, A. et al. Constraints on the superconducting order parameter in  $\text{Sr}_2\text{RuO}_4$  from oxygen-17 nuclear magnetic resonance. *Nature* **574**, 72-75 (2019).
- [6] Leggett, A. J. A theoretical description of the new phases of liquid  ${}^3\text{He}$ . *Rev. Mod. Phys.* **47**, 331-414 (1975).
- [7] Kojima, H. & Ishimoto, H. Spin polarized superfluid  ${}^3\text{He}$  A<sub>1</sub>. *J. Phys. Soc. Jpn.* **77**, 111001 (2008).
- [8] Huxley, A. et al. Realignment of the flux-line lattice by a change in the symmetry of superconductivity in  $\text{UPt}_3$ . *Nature* **406**, 160-164 (2000).
- [9] Lévy, F. et al. Magnetic field-induced superconductivity in the ferromagnet  $\text{URhGe}$ . *Science* **309**, 1343-1346 (2005).
- [10] Khim, S. et al. Field-induced transition within the superconducting state of  $\text{CeRh}_2\text{As}_2$ . *Science* **373**, 1012-1016 (2021).
- [11] Zheng, G. Q. et al. High temperature spin-triplet topological superconductivity in  $\text{K}_2\text{Cr}_3\text{As}_3$ . *J. Phys.: Conf. Ser.* **2545**, 012001 (2023).
- [12] Ran, S. et al. Nearly ferromagnetic spin-triplet superconductivity. *Science* **365**, 684-687 (2019).

[13] Aoki, D. et al. Unconventional superconductivity in heavy fermion UTe<sub>2</sub>. *J. Phys. Soc. Jpn.* **88**, 043702 (2019).

[14] Xu, Y., Sheng, Y. & Yang, Y. Quasi-two-dimensional Fermi surfaces and unitary spin- triplet pairing in the heavy fermion superconductor UTe<sub>2</sub>. *Phys. Rev. Lett.* **123**, 217002 (2019).

[15] Duan, C. et al. Resonance from antiferromagnetic spin fluctuations for superconductivity in UTe<sub>2</sub>. *Nature* **600**, 636-640 (2021).

[16] Hayes, I. M. et al. Multicomponent superconducting order parameter in UTe<sub>2</sub>. *Science* **373**, 797-801 (2021).

[17] Rosuel, A. et al. Field-induced tuning of the pairing state in a superconductor. *Phys. Rev. X* **13**, 011022 (2023).

[18] Wu, Z. et al. Enhanced triplet superconductivity in next-generation ultraclean UTe<sub>2</sub>. *Proc. Natl. Acad. Sci. USA* **121**, e2403067121 (2024).

[19] Wu, Z. et al. Superconducting critical temperature elevated by intense magnetic fields. *Proc. Natl. Acad. Sci. USA* **122**, e2422156122 (2025).

[20] Li, Z. et al. Observation of odd-parity superconductivity in UTe<sub>2</sub>. *Proc. Natl. Acad. Sci. USA* **122**, e2419734122 (2025).

[21] Lewin, S. K. et al. High-field superconducting halo in UTe<sub>2</sub>. *Science* **389**, 512-515 (2025).

[22] Wu, Z. et al. A quantum critical line bounds the high field metamagnetic transition surface in UTe<sub>2</sub>. *Phys. Rev. X* **15**, 021019 (2025).

[23] Ran, S. et al. Extreme magnetic field-boosted superconductivity. *Nat. Phys.* **15**, 1250-1254 (2019).

[24] Jiao, L. et al. Chiral superconductivity in heavy-fermion metal UTe<sub>2</sub>. *Nature* **579**, 523-527 (2020).

[25] Bae, S. et al. Anomalous normal fluid response in a chiral superconductor UTe<sub>2</sub>. *Nat. Commun.* **12**, 2644 (2021).

[26] Gu, Q. et al. Detection of a pair density wave state in UTe<sub>2</sub>. *Nature* **618**, 921-927 (2023).

[27] Thomas, S. M. et al. Evidence for a pressure-induced antiferromagnetic quantum critical point in intermediate-valence UTe<sub>2</sub>. *Sci. Adv.* **6**, eabc8709 (2020).

[28] Weinberger, T. I. et al. Strange metallicity encompasses high magnetic field-induced superconductivity in UTe<sub>2</sub>. *arXiv*: 2505.12131 (2025).

[29] Aoki, D. et al. Multiple superconducting phases and unusual enhancement of the upper critical

field in  $\text{UTe}_2$ . *J. Phys. Soc. Jpn.* **89**, 053705 (2020).

[30] Wu, Z. et al. Magnetic signatures of pressure-induced multicomponent superconductivity in  $\text{UTe}_2$ . *Phys. Rev. Lett.* **134**, 236501 (2025).

[31] Kinjo, K. et al. Superconducting spin reorientation in spin-triplet multiple superconducting phases of  $\text{UTe}_2$ . *Sci. Adv.* **9**, eadg2736 (2023).

[32] Matsumura, H. et al. Large reduction in the  $a$ -axis Knight shift on  $\text{UTe}_2$  with  $T_c = 2.1$  K. *J. Phys. Soc. Jpn.* **92**, 063701 (2023).

[33] Theuss, F. et al. Single-component superconductivity in  $\text{UTe}_2$  at ambient pressure. *Nat. Phys.* **20**, 1124-1130 (2024).

[34] Gu, Q. et al. Pair wave function symmetry in  $\text{UTe}_2$  from zero-energy surface state visualization. *Science* **388**, 938-944 (2025).

[35] Duif, A. M., Jansen, A. G. M. & Wyder, P. Point-contact spectroscopy. *J. Phys. Condens. Matter* **1**, 3157-3189 (1989).

[36] Deutscher, G. et al. Andreev-Saint-James reflections: A probe of cuprate superconductors. *Rev. Mod. Phys.* **77**, 109-135 (2005).

[37] Daghero, D. & Gonnelli, R. S. Probing multiband superconductivity by point-contact spectroscopy. *Supercond. Sci. Technol.* **23**, 043001 (2010).

[38] Sakai, H. et al. Single crystal growth of superconducting  $\text{UTe}_2$  by molten salt flux method. *Phys. Rev. Mater.* **6**, 073401 (2022).

[39] Eaton, A. G. et al. Quasi-2D Fermi surface in the anomalous superconductor  $\text{UTe}_2$ . *Nat. Commun.* **15**, 223 (2024).

[40] Tanaka, Y. & Kashiwaya, S. Theory of tunneling spectroscopy of  $d$ -wave superconductors. *Phys. Rev. Lett.* **74**, 3451 (1995).

[41] Daghero, D. et al. Strong-coupling  $d$ -wave superconductivity in  $\text{PuCoGa}_5$  probed by point-contact spectroscopy. *Nat. Commun.* **3**, 786 (2012).

[42] Sheet, G., Mukhopadhyay, S. & Raychaudhuri, P. Role of critical current on the point-contact Andreev reflection spectra between a normal metal and a superconductor. *Phys. Rev. B* **69**, 134507 (2004).

[43] Naidyuk, Y. G. & Yanson, I. K. *Point-contact Spectroscopy* (Springer, 2004).

[44] Sasaki, S. et al. Topological superconductivity in  $\text{Cu}_x\text{Bi}_2\text{Se}_3$ . *Phys. Rev. Lett.* **107**, 217001 (2011).

- [45] Appelbaum, J. A. Exchange model of zero-bias tunneling anomalies. *Phys. Rev.* **154**, 633-643 (1967).
- [46] Shen, L. Y. L. & Rowell, J. M. Zero-bias tunneling anomalies-temperature, voltage, and magnetic field dependence. *Phys. Rev.* **165**, 566-577 (1968).
- [47] Yoon, H. et al. Probing *p*-wave superconductivity in UTe<sub>2</sub> via point-contact junctions. *npj Quantum Mater.* **9**, 91 (2024).
- [48] Suetsugu, S. et al. Fully gapped pairing state in spin-triplet superconductor UTe<sub>2</sub>. *Sci. Adv.* **10**, eadk3772 (2024).

## ACKNOWLEDGEMENTS

This work is supported by the National Key R&D Program of China (2023YFA1609600, 2022YFA1602602, and 2022YFA1402200), National Natural Science Foundation of China (U23A20580, 12374042, 12174333 and 12574147), Beijing National Laboratory for Condensed Matter Physics (2024BNLCMPKF004). A portion of this work was carried out at the Synergetic Extreme Condition User Facility (SECUF, <https://cstr.cn/31123.02.SECUF>). W.H. acknowledges a start-up fund at Great Bay University. A.G.E. acknowledges support from the Henry Royce Institute for Advanced Materials through the Equipment Access Scheme enabling access to the Advanced Materials Characterisation Suite at Cambridge (EP/P024947/1, EP/M000524/1, and EP/R00661X/1).

## AUTHOR CONTRIBUTIONS

Y.L., X.L. and H.Y. conceived and designed the experiments. Z.W., A.C., M.V., N.L., B.Z., A.G.E. and C.Z. grew and characterized high-quality single crystalline samples. S.Z., F.S. performed most of the experiments with the aids from Y.Z., W.Q., Z.W., H.Z., Y.M., Z.Y., K.Y., Jiawen Z., Y.Z., K.L., G.L. and J.L. S.Z. and Z.Q. carried out numerical simulations and fittings with the aids from Jialong Z. and W.H. S.Z., Z.Q., W.H., X.L., H.Y. and Y.L. discussed the data, interpreted the results, and wrote the paper with input from all the authors.

## COMPETING INTERESTS

The authors declare no competing interests.

## **ADDITIONAL INFORMATION**

**Supplementary information** The online version contains supplementary material available at \*\*\*\*\*

**Correspondence** and requests for materials should be addressed to Wen Huang, Huiqiu Yuan, Xin Lu or Yongkang Luo.

**Reprints and permission information** is available at  
<http://www.nature.com/reprints>

**Publisher's note** Springer Nature remains neutral with regard to jurisdictional claims in published maps and institutional affiliations.

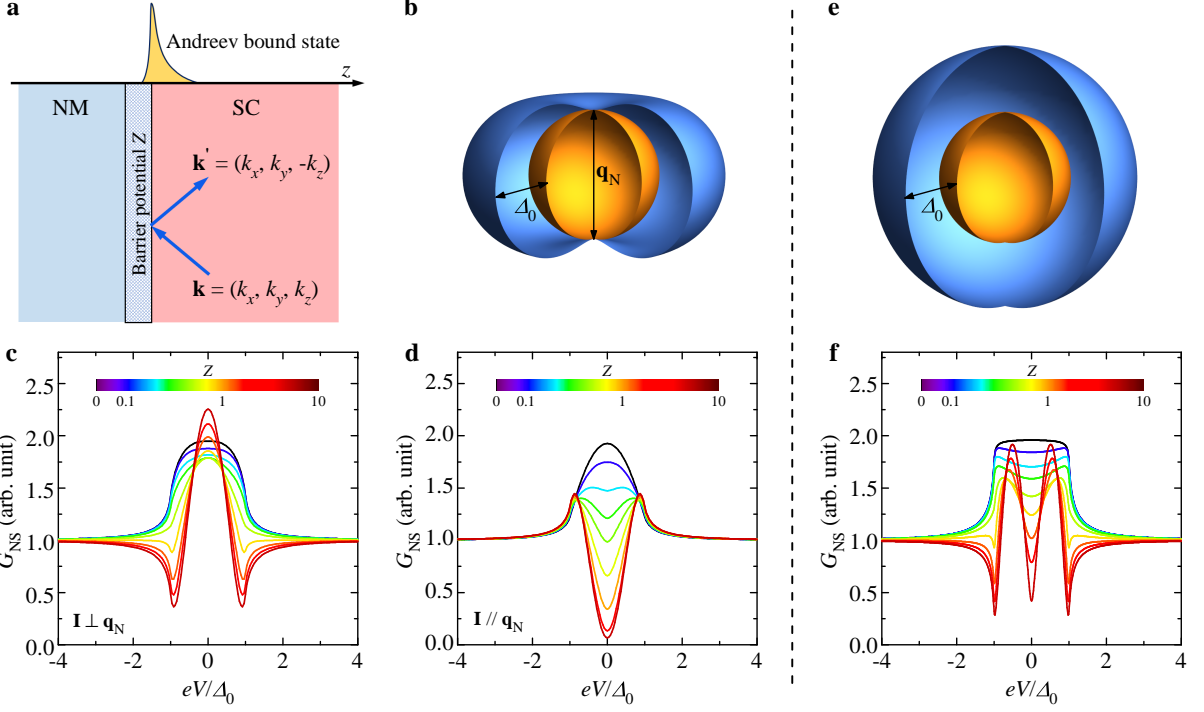


**Figure 1 | Gap structure and Andreev bound state (ABS) in unconventional superconductors.** **a** A cartoon illustration of the reflection of Cooper pairs at the boundary (characterized by a barrier potential  $Z$ ) of a superconductor that changes the scattering wavevector  $\mathbf{k} = (k_x, k_y, k_z)$  into  $\mathbf{k}' = (k_x, k_y, -k_z)$ . If the SC gap function  $[\Delta(\mathbf{k})]$  changes sign upon taking  $k_z$  to  $-k_z$ , an ABS will be trapped near the boundary. **b** Nodal gap structure with maximum  $\Delta_0$ . The internodal scattering is denoted by the wavevector  $\mathbf{q}_N$ . **c** For tunneling current  $\mathbf{I} \perp \mathbf{q}_N$ , the sign change in  $\Delta(k_z) \rightarrow \Delta(-k_z)$  leads to the formation of zero-energy ABS (ZABS) and hence a sharp zero-bias conductance peak (ZBCP) in the differentiate conductance ( $G_{\text{NS}}$ ) that readily exceeds 2 in the large- $Z$  limit. **d** Such a ZABS is absent if the tunneling current is along  $\mathbf{q}_N$ . **e** Sketch of a fully-gapped structure, e.g.  $A_u$  representation. **f**  $G_{\text{NS}}$  does not exhibit a ZABS in this case; instead, a pronounced dip is expected at zero bias at large  $Z$ .

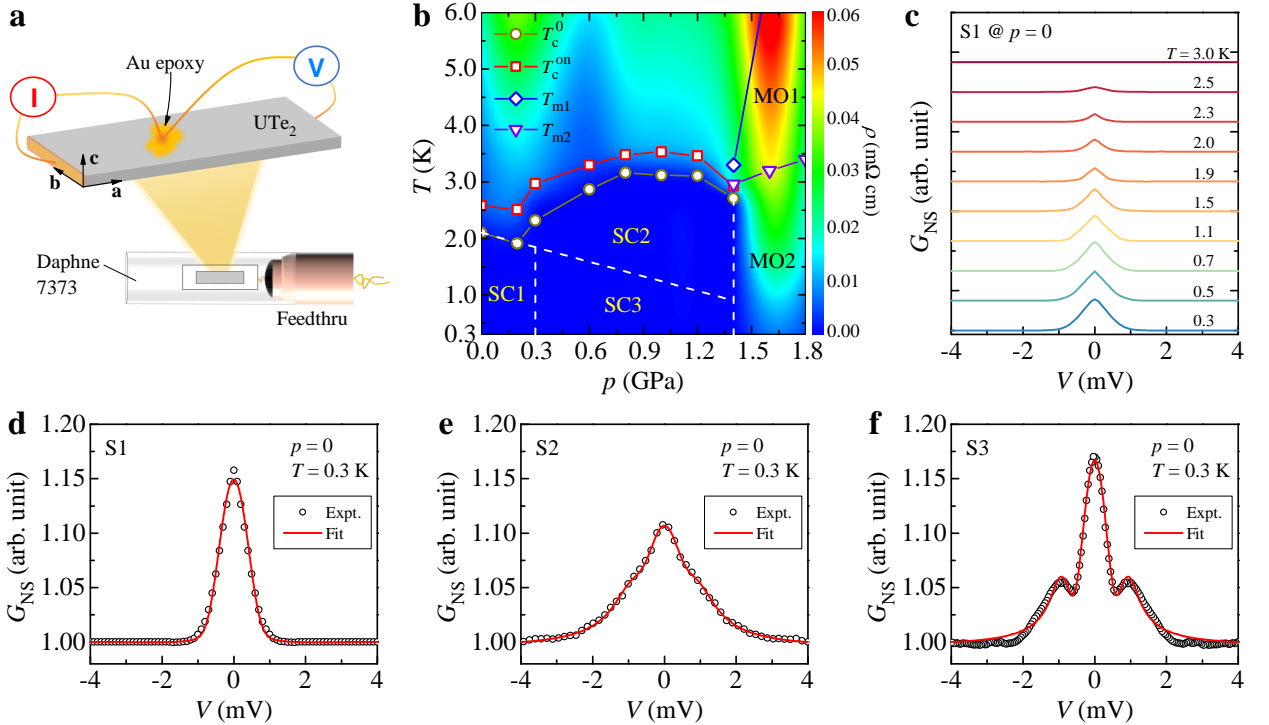


**Figure 2 | Point-contact spectroscopy (PCS) of  $\text{UTe}_2$  at ambient pressure.** **a** A sketch of point contact spectroscopy measurement under pressure. The junction is made on the (0 0 1) plane. **b** Phase diagram of  $\text{UTe}_2$  constructed by a contour plot of  $\rho(p, T)$ . The dashed lines are reproduced from previous specific heat and magnetic susceptibility studies [27, 29, 30]. These dashed lines divide the SC region into three possible phases, SC1-3. **c** The differential conductance ( $G_{\text{NS}}$ ) of sample S1 at various temperatures. The curves are shifted vertically for clarity. **d-f**  $G_{\text{NS}}$  at 0.3 K for samples S1, S2 and S3, respectively. The red lines are fittings of the experimental data (open circles) to the extended BTK model in  $B_{2u}$  (or  $B_{3u}$ ) representation. The obtained fitting parameters are summarized in Table S1.

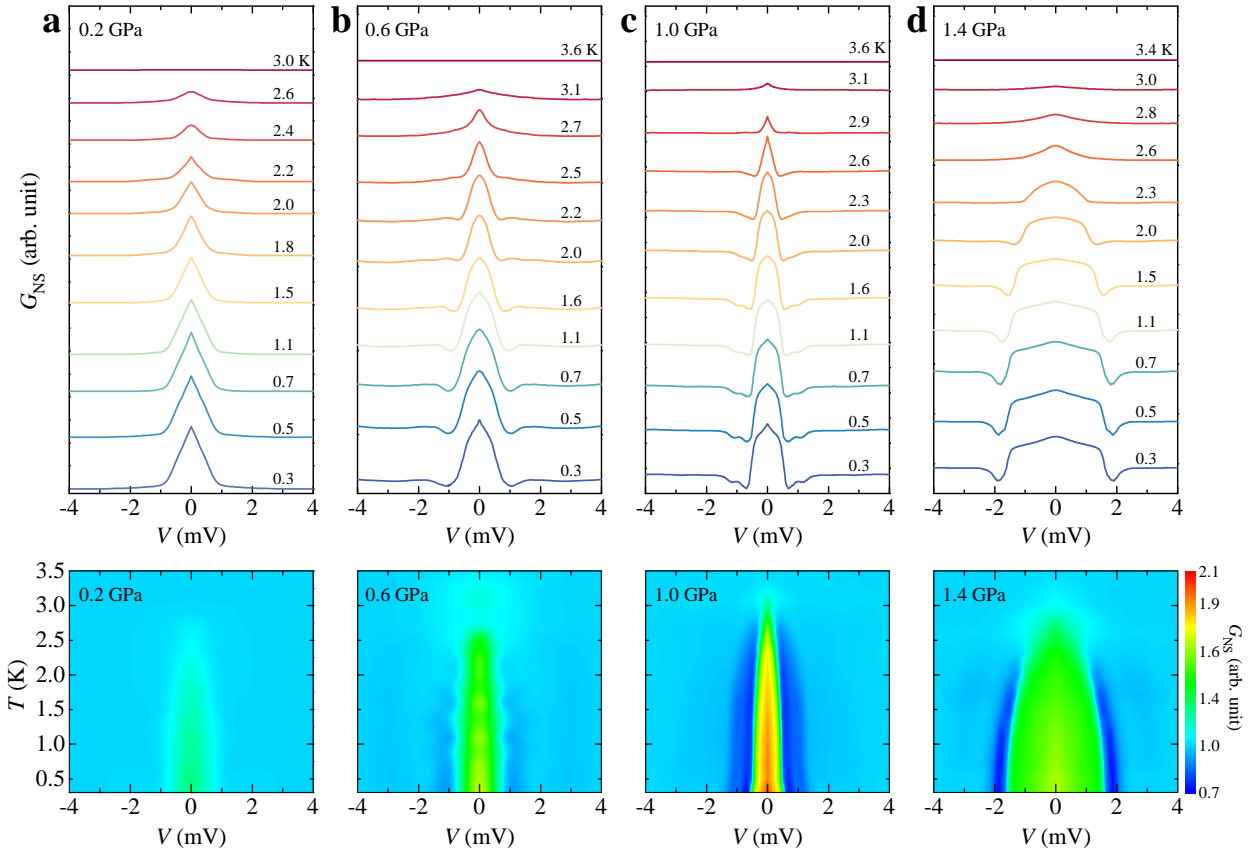


**Figure 3 | Point-contact spectroscopy (PCS) of  $\text{UTe}_2$  under pressure.** Upper panels, differential conductance ( $G_{\text{NS}}$ ) at selected pressures, **a** 0.2 GPa; **b** 0.6 GPa; **c** 1.0 GPa; and **d** 1.4 GPa. The lower panels display the false-color contour plots of  $G_{\text{NS}}(V, T)$ .

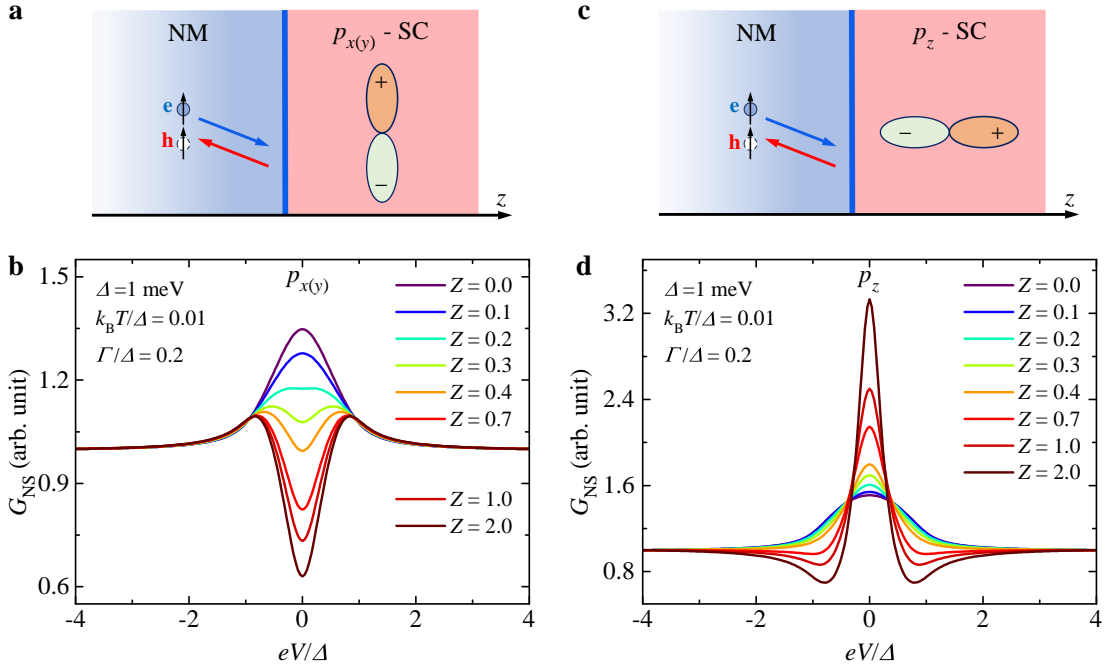


**Figure 4 | Simulation of Point-contact Andreev reflection spectroscopy based on the extended Blonder-Tinkham-Klapwijk (BTK) model. a-b**  $p_{x(y)}$  pairing symmetry. **c-d**  $p_z$  pairing symmetry. The simulations were performed with  $\Delta = 1 \text{ meV}$ ,  $k_B T/\Delta = 0.01$ ,  $\Gamma/\Delta = 0.2$ , and variable  $Z$  listed in the figures.

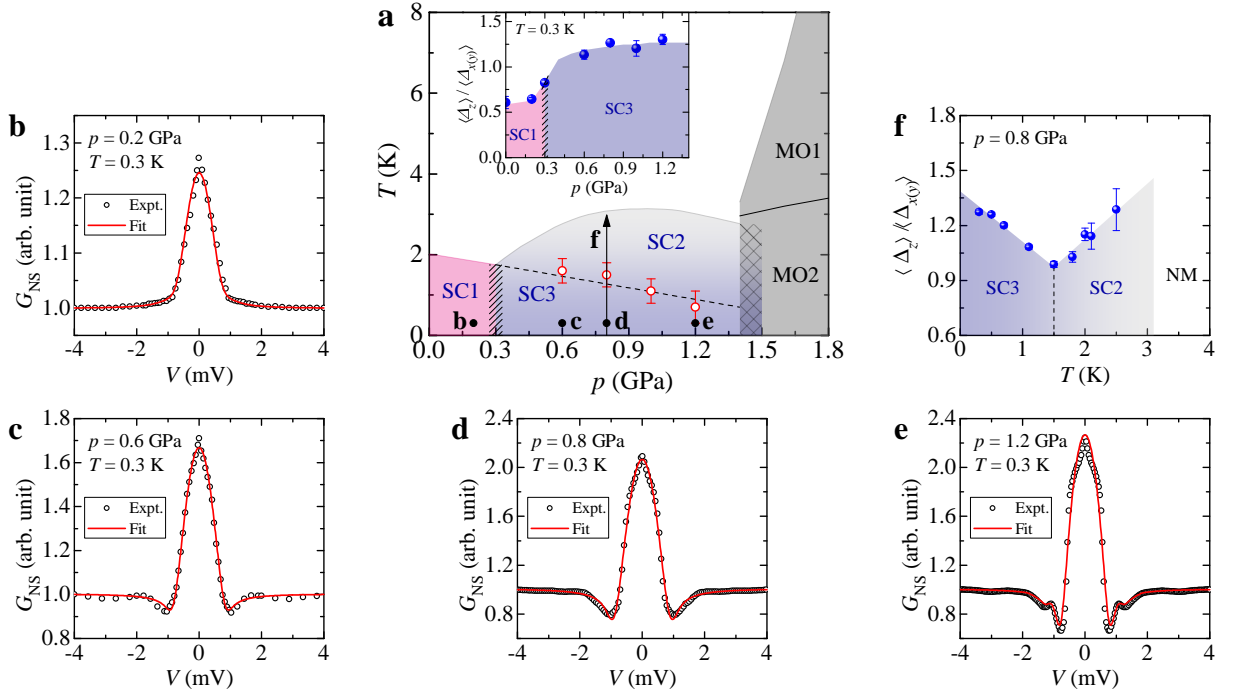


**Figure 5 | Blonder-Tinkham-Klapwijk fittings of the Point-contact spectroscopy (PCS) in different regions.** **a** Schematic phase diagram of  $\text{UTe}_2$  under pressure. The boundaries of the phase diagram are generally reproduced from Fig. 2(b). The dashed line is a guide to eyes to mark the transition between SC2 and SC3 determined by earlier AC calorimetry and AC magnetic susceptibility measurements [27, 30]. The red open circles represent the critical temperatures defined as the minimum of iso-pressure temperature dependent  $\langle \Delta_z \rangle / \langle \Delta_{x(y)} \rangle$ , as exemplified by the results at 0.8 GPa in panel **f**. The inset presents  $\langle \Delta_z \rangle / \langle \Delta_{x(y)} \rangle$  at 0.3 K as a function of  $p$ , which reveals an abrupt increase in the weight of  $p_z$ -wave pairing from SC1 to SC3. **b** Fitting for  $p = 0.2$  GPa and  $T = 0.3$  K. **c** Fitting for  $p = 0.6$  GPa and  $T = 0.3$  K. **d** Fitting for  $p = 0.8$  GPa and  $T = 0.3$  K. **e** Fitting for  $p = 1.2$  GPa and  $T = 0.3$  K. **f**  $\langle \Delta_z \rangle / \langle \Delta_{x(y)} \rangle$  as a function of  $T$  at fixed pressure  $p = 0.8$  GPa.

**Supplementary Information:  
Multiple nodal superconducting phases and order-parameter  
evolution in pressurized  $\text{UTe}_2$**

Shuo Zou<sup>1\*</sup>, Fengrui Shi<sup>2\*</sup>, Zhuolun Qiu<sup>1\*</sup>, Jialong Zhang<sup>3</sup>, Yan Zhang<sup>2</sup>, Weilong Qiu<sup>2</sup>, Zhuo Wang<sup>1</sup>, Hai Zeng<sup>1</sup>, Yinina Ma<sup>4</sup>, Zheyu Wu<sup>5</sup>, Andrej Cabala<sup>6</sup>, Michal Vališka<sup>6</sup>, Ning Li<sup>7</sup>, Zihan Yang<sup>2</sup>, Kaixin Ye<sup>2</sup>, Jiawen Zhang<sup>2</sup>, Yanan Zhang<sup>2</sup>, Kangjian Luo<sup>1</sup>, Binbin Zhang<sup>7</sup>, Alexander G. Eaton<sup>5</sup>, Chaofan Zhang<sup>7</sup>, Gang Li<sup>4</sup>, Jianlin Luo<sup>4</sup>, Wen Huang<sup>3†</sup>, Huiqiu Yuan<sup>2‡</sup>, Xin Lu<sup>2§</sup>, and Yongkang Luo<sup>1¶</sup>

<sup>1</sup> *Wuhan National High Magnetic Field Center and School of Physics, Huazhong University of Science and Technology, Wuhan 430074, China;*

<sup>2</sup> *Center for Correlated Matter and School of Physics, Zhejiang University, Hangzhou 310058, China;*

<sup>3</sup> *School of Physical Sciences, Great Bay University, Dongguan 523000, China;*

<sup>4</sup> *Beijing National Laboratory for Condensed Matter Physics, Institute of Physics, Chinese Academy of Sciences, Beijing 100190, China;*

<sup>5</sup> *Cavendish Laboratory, University of Cambridge, Cambridge CB3 0HE, United Kingdom;*

<sup>6</sup> *Charles University, Faculty of Mathematics and Physics, Department of Condensed Matter Physics, Prague 2 121 16, Czech Republic;*

<sup>7</sup> *College of Advanced Interdisciplinary Studies and Nanhu Laser Laboratory, National University of Defense Technology, Changsha, Hunan 410073, China;*

In this **Supplementray Information (SI)**, we provide more results that will further support the discussions and conclusion in the main text, including additional resistivity and point-contact spectroscopy (PCS) data under pressure, simulations of Andreev PCS and fittings to the experimental data.

## SI I: Resistivity results of $\text{UTe}_2$ under pressure

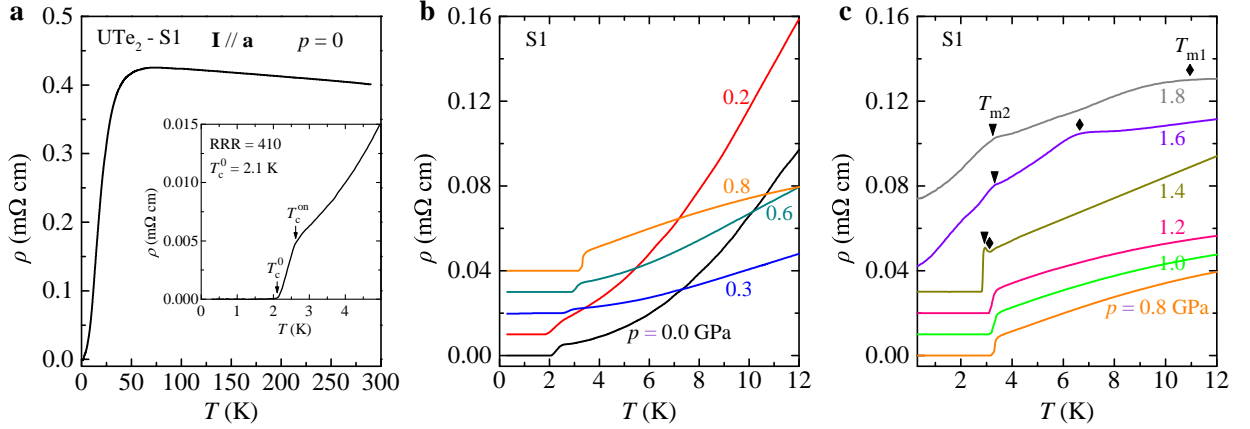


**Figure S1 | Resistivity data of  $\text{UTe}_2$  (sample S1) under pressure.** Measured with electrical current  $\mathbf{I} \parallel \mathbf{a}$ . **a** Main frame, electrical resistivity ( $\rho$ ) as a function of  $T$  at ambient pressure. Inset, the zoom-in plot to show the superconducting transition at low temperature. The sample is of good quality with residual resistance ratio (RRR)  $\sim 410$ , and SC transition temperatures  $T_c^{\text{on}} = 2.6$  K and  $T_c^0 = 2.1$  K. **b** and **c**  $\rho(T)$  profiles for under pressure. The curves are vertically shifted for clarity. The black triangles and diamonds denote the characteristic temperatures ( $T_{\text{m1}}$  and  $T_{\text{m2}}$ ) of the two magnetically ordered phases MO1 and MO2, respectively.

## SI II: Additional PCS results at ambient pressure

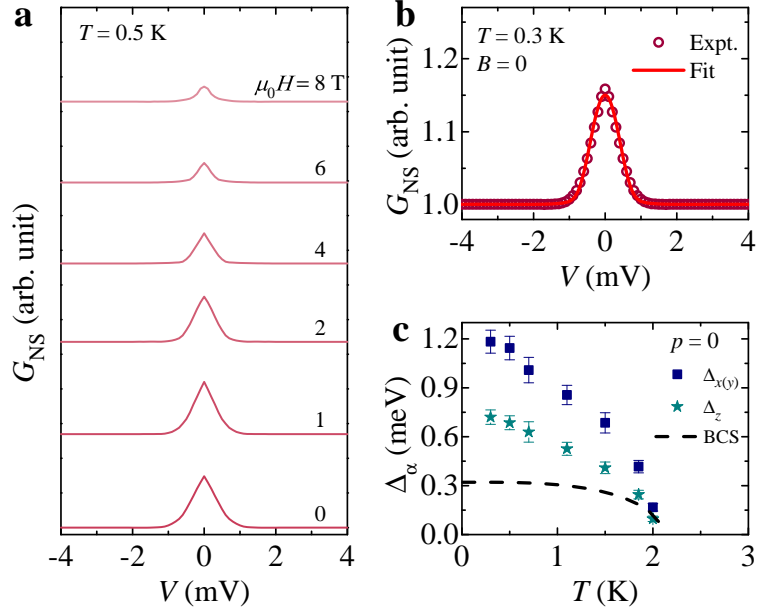


**Figure S2 | Additional Point-contact Andreev reflection spectroscopy of  $\text{UTe}_2$  at ambient pressure.** **a** Isothermal  $G_{\text{NS}}(V)$  under different magnetic field for fixed temperature  $T = 0.5$  K. **b** Representative fitting of the  $dI/dV$  spectrum to the extended Blonder-Tinkham-Klapwijk (BTK) model, taking  $T = 0.3$  K as an example. **c** The obtained gap parameters  $\Delta_{x(y)}$  and  $\Delta_z$  as functions of  $T$ . They apparently deviates from the conventional Bardeen-Cooper-Schrieffer (BCS) behavior, strongly suggesting unconventional superconductivity.

### SI III: Additional PCS results under pressure

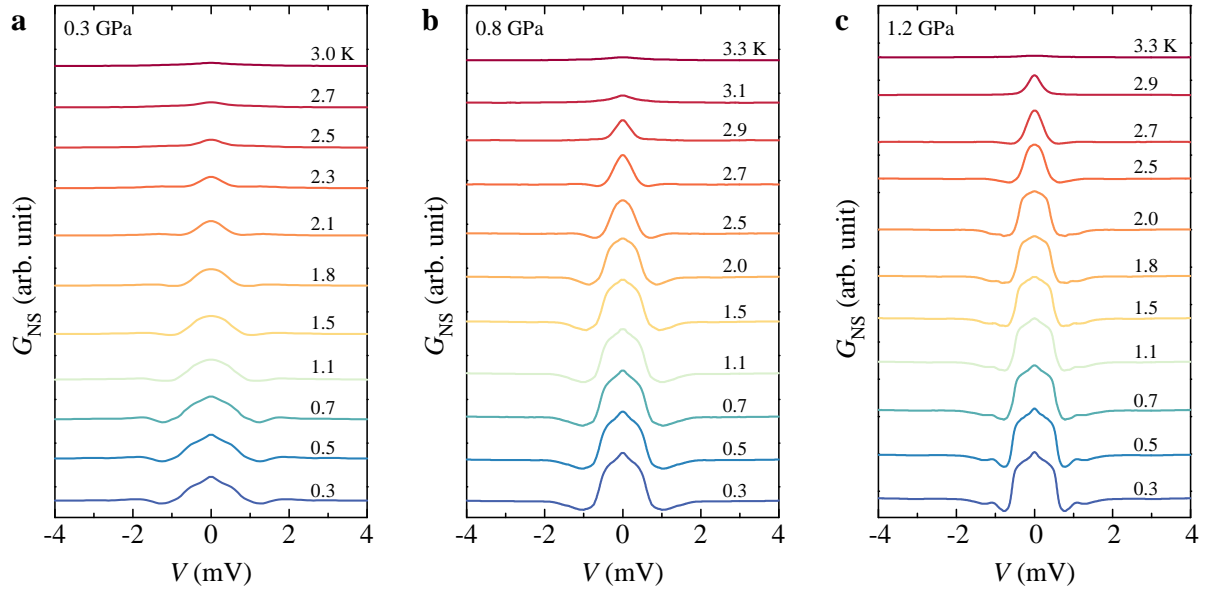


**Figure S3 | Additional Point-contact Andreev reflection spectroscopy data of  $\text{UTe}_2$  under pressure.** The differential conductance ( $G_{\text{NS}}$ ) at various temperatures. **a** 0.3 GPa. **b** 0.8 GPa. **c** 1.2 GPa. The curves are shifted vertically for clarity.

## SI IV: Extended BTK model for spin-triplet superconductivity

In this section, we provide the details to deduce the expression of differential conductance ( $G_{\text{NS}} = dI/dV$ ) of Andreev reflection PCS for a junction between normal metal and superconductor (NM-SC), as sketched in Fig. S4(a). Andreev reflection refers to a scattering process that an electron incident on the interface from the NM is retro-reflected as a hole by creating a Cooper pair in the SC [1]. For spin-triplet SCs, the process of Andreev reflection is more complex compared with that of conventional spin-singlet counterparts due to the increase of the reflection channels. For instance, if the incident particle is a spin-up electron, the reflected particle could be either a spin-up hole through the channel of equal-spin Cooper pair  $\Phi_{+1} = |\uparrow\uparrow\rangle$ , or a spin-down hole through the channel of opposite-spin Cooper pair  $\Phi_0 = (|\uparrow\downarrow\rangle + |\downarrow\uparrow\rangle)/\sqrt{2}$ , as depicted in Fig. S4(b). The Blonder-Tinkham-Klapwijk (BTK) model provides a theoretical framework for analyzing the Andreev reflection PCS [2], which is based on the Bogoliubov-de Gennes (BdG) method.

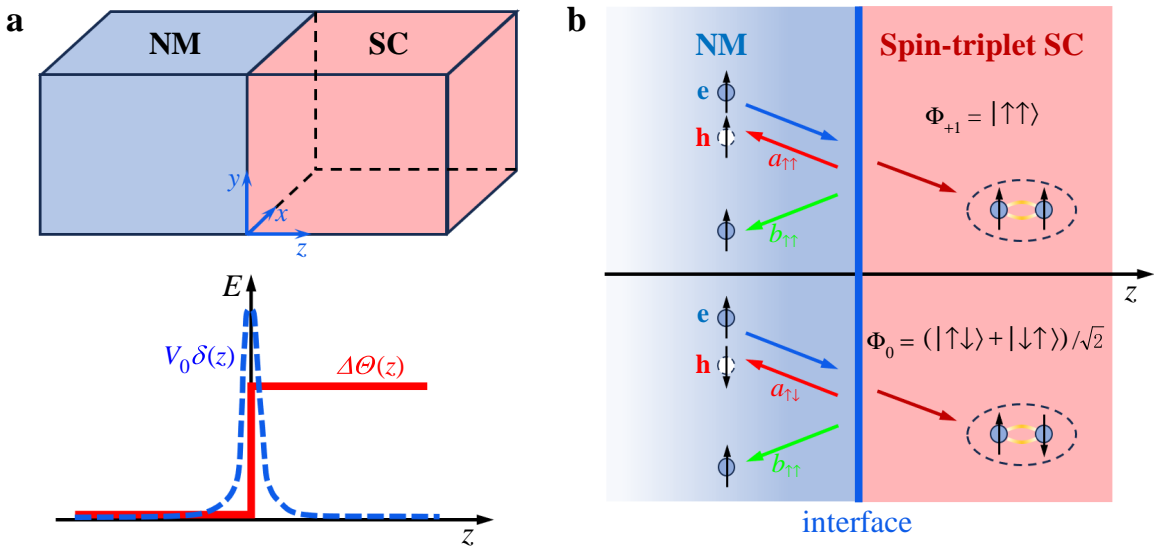


**Figure S4 | Schematics of Andreev reflection at the interface of normal metal (NM) and superconductor (SC).** **a** Sketch of the NM-SC junction. In this work, the junction is made by Au-UTe<sub>2</sub>, on the **x**-**y** crystallographic plane of UTe<sub>2</sub>. **b** Andreev reflection (red arrows,  $a_{\alpha\beta}$ ) for spin-triplet SC. For an electron (blue circle) incident at the interface, a hole (open circle) is retro-reflected by creating a Cooper pair in the SC. Note that the spin state of the reflected hole relies on the specific configuration of the Cooper pair. The green arrows denote the normal specular reflection ( $b_{\alpha\beta}$ ) that preserves spin degree of freedom.

In this work, the NM-SC junction lies in the **x**-**y** plane (or **a**-**b** crystallographic plane),

with a potential barrier  $V_0\delta(z)$  at the interface  $z = 0$ . The NM sits at the region  $z < 0$ , while the spin-triplet SC resides in  $z > 0$ .

The BdG equation that governs the system is given by [3]

$$\check{H}_{\text{BTK}}(\mathbf{r})\Phi(\mathbf{r}) = E\Phi(\mathbf{r}), \quad (\text{S1})$$

where  $\check{H}_{\text{BTK}}(\mathbf{r}) = \begin{bmatrix} \xi(\mathbf{r})\hat{\sigma}_0 & \hat{\Delta}(\mathbf{r}) \\ \hat{\Delta}^\dagger(\mathbf{r}) & -\xi(\mathbf{r})\hat{\sigma}_0 \end{bmatrix}$ ,  $\xi(\mathbf{r}) = -\frac{\hbar^2\nabla^2}{2m} + V_0\delta(z) - \varepsilon_F$ ,  $\hat{\Delta}(\mathbf{r}) = \hat{\Delta}e^{i\varphi}\Theta(z)$ .  $\varepsilon_F$  is the Fermi energy of the system, and  $\hat{\sigma}_0$  is the  $2 \times 2$  identity matrix. The gap matrix for a spin-triplet SC is defined as  $\hat{\Delta}(\mathbf{k}) = i\mathbf{d}(\mathbf{k}) \cdot \hat{\sigma}\hat{\sigma}_2$ , where  $\mathbf{d} = (d_1, d_2, d_3)$  is the vector that describes the pairing states of electrons, and  $\hat{\sigma} = (\hat{\sigma}_1, \hat{\sigma}_2, \hat{\sigma}_3)$  with  $\hat{\sigma}_i$  ( $i = 1, 2, 3$ ) being the Pauli matrix. We here assume  $\mathbf{d} \times \mathbf{d}^* = 0$ , which denotes that the gap matrix is unitary [3].

The wave function in the NM region can be expressed as [4]

$$\Phi_{N\alpha}(\mathbf{r}) = \sum_{|\mathbf{k}_\parallel| < k_F} \left[ \begin{pmatrix} \delta_{\alpha\uparrow} \\ \delta_{\alpha\downarrow} \\ 0 \\ 0 \end{pmatrix} e^{ik_z z} + \begin{pmatrix} b_{\alpha\uparrow} \\ b_{\alpha\downarrow} \\ 0 \\ 0 \end{pmatrix} e^{-ik_z z} + \begin{pmatrix} 0 \\ 0 \\ a_{\alpha\uparrow} \\ a_{\alpha\downarrow} \end{pmatrix} e^{ik_z z} \right] \cdot f_{\mathbf{k}_\parallel}(\boldsymbol{\rho}), \quad (\text{S2})$$

where  $\delta_{\alpha\beta}$  is the Kronecker symbol, while  $a_{\alpha\beta}$  and  $b_{\alpha\beta}$  stand for the Andreev reflection and normal reflection coefficients, respectively [Fig. S4(b)]. The subscript indices  $\alpha$  and  $\beta$  denote the spin state. The spatial wave function parallel to the junction interface is expressed as  $f_{\mathbf{k}_\parallel}(\boldsymbol{\rho}) = e^{i\mathbf{k}_\parallel \cdot \boldsymbol{\rho}}/\sqrt{S}$ , where  $S$  is area of the interface. The displacement vector  $\boldsymbol{\rho} = (x, y, 0)$  lies within the interfacial plane and the wave vector component parallel to the junction interface is given by  $\mathbf{k}_\parallel = (k_x, k_y, 0)$ . For those particles with energy  $E \ll \varepsilon_F$ , the wave vector components obey the approximate relation  $k_z^2 + |\mathbf{k}_\parallel|^2 \approx k_F^2 = \sqrt{\frac{2m\varepsilon_F}{\hbar^2}}$ .

The wave function in the SC is given by [3]

$$\Phi_{S\alpha}(\mathbf{r}) = \sum_{|\mathbf{k}_\parallel| < k_F} \left[ c_{\alpha 1}^{(e)} \begin{pmatrix} u_+ \\ 0 \\ -\tilde{d}_{1,+}^* - i\tilde{d}_{2,+}^* \\ \tilde{d}_{3,+}^* \end{pmatrix} e^{ik_z z} + c_{\alpha 2}^{(e)} \begin{pmatrix} 0 \\ u_+ \\ \tilde{d}_{3,+}^* \\ \tilde{d}_{1,+}^* - i\tilde{d}_{2,+}^* \end{pmatrix} e^{ik_z z} \right. \right. \\ \left. \left. + c_{\alpha 1}^{(h)} \begin{pmatrix} -\tilde{d}_{1,-} + i\tilde{d}_{2,-} \\ \tilde{d}_{3,-} \\ u_- \\ 0 \end{pmatrix} e^{-ik_z z} + c_{\alpha 2}^{(h)} \begin{pmatrix} \tilde{d}_{3,-} \\ \tilde{d}_{1,-} + i\tilde{d}_{2,-} \\ 0 \\ u_- \end{pmatrix} e^{-ik_z z} \right] \cdot f_{\mathbf{k}_\parallel}(\boldsymbol{\rho}), \quad (S3) \right.$$

where

$$u_\pm = \frac{E + \xi_\pm}{\sqrt{(E + \xi_\pm)^2 + |\mathbf{d}_\pm|^2}}, \quad \tilde{d}_{i,\pm} = \frac{d_{i,\pm}}{\sqrt{(E + \xi_\pm)^2 + |\mathbf{d}_\pm|^2}}, \\ \xi_\pm = \sqrt{E^2 - |\mathbf{d}_\pm|^2}, \quad \mathbf{d}_\pm = \mathbf{d}(\pm k_z, \mathbf{k}_\parallel) = (d_{1,\pm}, d_{2,\pm}, d_{3,\pm}),$$

and  $c_{\alpha i}^{(e(h))}$  represents the transmission coefficient for an electron-like (hole-like) quasiparticle. Notably, the kinetic energy of quasiparticle,  $\xi = \sqrt{E^2 - |\mathbf{d}(\mathbf{k})|^2}$ , satisfies the following relation, due to the causality of the transport coefficients [5]

$$\xi = \begin{cases} \sqrt{E^2 - |\mathbf{d}(\mathbf{k})|^2}, & (E \geq |\mathbf{d}(\mathbf{k})|) \\ i\sqrt{|\mathbf{d}(\mathbf{k})|^2 - E^2}, & (-|\mathbf{d}(\mathbf{k})| < E < |\mathbf{d}(\mathbf{k})|) \\ -\sqrt{E^2 - |\mathbf{d}(\mathbf{k})|^2}. & (E \leq -|\mathbf{d}(\mathbf{k})|) \end{cases} \quad (S4)$$

The boundary conditions for the wave functions are [5]

$$\Phi_{S\alpha}(\mathbf{r})|_{z=0^+} = \Phi_{N\alpha}(\mathbf{r})|_{z=0^-}, \quad (S5)$$

$$-\frac{\hbar^2}{2m} [\partial_z \Phi_{S\alpha}(\mathbf{r})|_{z=0^+} - \partial_z \Phi_{N\alpha}(\mathbf{r})|_{z=0^-}] + V_0 \Phi_{S\alpha}(\mathbf{r})|_{z=0^+} = 0, \quad (S6)$$

where  $m$  is the mass of the electron. The boundary conditions are derived from the continuity of the wave function and the conservation of the probability current density, respectively.

Substituting the wave functions Eqs. (S2) and (S3) into two boundary conditions, we

can derive the following equations:

$$\begin{pmatrix} \hat{\sigma}_0 \\ \hat{R}_h \end{pmatrix} = \check{U} \begin{pmatrix} (1 + i \frac{Z}{\tilde{k}}) \hat{T}_e \\ i \frac{Z}{\tilde{k}} \hat{T}_h \end{pmatrix}, \quad (\text{S7})$$

$$\begin{pmatrix} \hat{R}_e \\ 0 \end{pmatrix} = \check{U} \begin{pmatrix} -i \frac{Z}{\tilde{k}} \hat{T}_e \\ (1 - i \frac{Z}{\tilde{k}}) \hat{T}_h \end{pmatrix}, \quad (\text{S8})$$

where

$$\check{U} = \begin{bmatrix} u_+ \hat{\sigma}_0 & \hat{v}_- \\ \hat{v}_+ & u_- \hat{\sigma}_0 \end{bmatrix}, \quad \hat{v}_+ = \frac{\hat{\Delta}_+^\dagger}{\sqrt{(E + \xi_+)^2 + |\mathbf{d}_+|^2}},$$

$$\hat{v}_- = \frac{\hat{\Delta}_-}{\sqrt{(E + \xi_-)^2 + |\mathbf{d}_-|^2}}, \quad \hat{\Delta}_\pm = \hat{\Delta}(\pm k_z, \mathbf{k}_\parallel), \quad Z = \frac{mV_0}{\hbar^2 k_F}, \quad \tilde{k} = \frac{k_z}{k_F}.$$

$\hat{R}_h = \begin{bmatrix} a_{\uparrow\uparrow} & a_{\uparrow\downarrow} \\ a_{\uparrow\downarrow} & a_{\downarrow\downarrow} \end{bmatrix}$  is the Andreev reflection matrix,  $\hat{R}_e = \begin{bmatrix} b_{\uparrow\uparrow} & b_{\uparrow\downarrow} \\ b_{\uparrow\downarrow} & b_{\downarrow\downarrow} \end{bmatrix}$  is the normal reflection matrix, and  $\hat{T}_{e(h)} = \begin{bmatrix} c_{\uparrow 1}^{(e(h))} & c_{\downarrow 1}^{(e(h))} \\ c_{\uparrow 2}^{(e(h))} & c_{\downarrow 2}^{(e(h))} \end{bmatrix}$  is the transmission matrix of electron-like (hole-like) quasiparticles, respectively.

By solving Eqs. (S7) and (S8), we can get solutions for the reflection matrix:

$$\hat{R}_e = r_n \left( 1 - \frac{\hat{v}_- \hat{v}_+}{u_+ u_-} \right) \hat{A}^{-1}, \quad \hat{R}_h = |t_n|^2 \frac{\hat{v}_+}{u_+} \hat{A}^{-1} \quad (\text{S9})$$

where  $r_n = \frac{-iZ}{\tilde{k} + iZ}$ ,  $t_n = \frac{\tilde{k}}{\tilde{k} + iZ}$ ,  $\hat{A} = 1 - |r_n|^2 \frac{\hat{v}_- \hat{v}_+}{u_+ u_-}$ .

Total current across the NM-SC junction deduced from the Landauer-Büttiker expression is given by [6]

$$I_{\text{NS}} = I_0 \int_{-\infty}^{+\infty} [f_L(E) - f_R(E)] \sum_{\mathbf{k}_\parallel} \left\{ 1 + \frac{1}{2} \sum_{\alpha, \beta} [|a_{\alpha\beta}(E)|^2 - |b_{\alpha\beta}(E)|^2] \right\} dE, \quad (\text{S10})$$

where  $f_{L(R)}(E) = (1 + e^{E - \mu_{L(R)}/k_B T})^{-1}$  is the Fermi-Dirac distribution function of the left (right) reservoirs with the chemical potentials  $\mu_L = \varepsilon_F + eV$  and  $\mu_R = \varepsilon_F$ , respectively.

The reflection coefficients satisfy

$$\sum_{\alpha,\beta} \{|b_{\alpha\beta}(E)|^2 = \text{Tr}(\hat{R}_e \hat{R}_e^\dagger), \sum_{\alpha,\beta} \{|a_{\alpha\beta}(E)|^2 = \text{Tr}(\hat{R}_h \hat{R}_h^\dagger)\}. \quad (\text{S11})$$

Then, with the Andreev reflection and normal reflection coefficients, the differential conductance (as a function of  $V$  and  $T$ ) is given by

$$G_{\text{NS}}(V, T) = \frac{d}{dV} I_{\text{NS}} = G_0 \int_{-\infty}^{+\infty} \frac{\partial f(E - eV)}{\partial V} \sum_{\mathbf{k}_\parallel} \left\{ 1 + \frac{1}{2} \sum_{\alpha,\beta} [|a_{\alpha\beta}(E)|^2 - |b_{\alpha\beta}(E)|^2] \right\} dE, \quad (\text{S12})$$

Specially, at zero temperature, the differential conductance is obtained,

$$G_{\text{NS}}(V)|_{T=0} = G_0 \left\{ 1 + \frac{1}{2} \sum_{\alpha,\beta} [|a_{\alpha\beta}(eV)|^2 - |b_{\alpha\beta}(eV)|^2] \right\}. \quad (\text{S13})$$

A detailed solution of the BdG equations in the presence of inelastic scattering [7] shows that the impact of finite quasiparticle lifetime can be effectively modeled through the substitution  $E \rightarrow E + i\Gamma$ . This leads us to the final expression for the differential conductance in this model,

$$G_{\text{NS}}(V, T) = G_0 \int_{-\infty}^{+\infty} \frac{\partial f(E - eV)}{\partial V} \sum_{\mathbf{k}_\parallel} \left\{ 1 + \frac{1}{2} \sum_{\alpha,\beta} [|a_{\alpha\beta}(E + i\Gamma)|^2 - |b_{\alpha\beta}(E + i\Gamma)|^2] \right\} dE. \quad (\text{S14})$$

## SI V: Simulations of Andreev reflection PCS for spin-triplet superconductivity

Figure S5 shows the simulated PCS at different temperatures, based on  $p_{x(y)}$ - (left column) and  $p_z$ - (right column) wave pairings. For comparison, all the simulations were performed with fixed  $\Gamma/\Delta = 0.2$ . For small  $Z = 0.2$ , both  $p_{x(y)}$  and  $p_z$  waves show peak-like feature at zero bias, as shown in Fig. S5(a,c). For large  $Z = 1$ , they differ to each other substantially. For  $p_{x(y)}$  wave, a zero-bias dip develops [Fig. S5(a)]. In contrast, for  $p_z$  wave, the ZBCP is robust against varying  $Z$ , but meanwhile a dip develops on each side of the ZBCP, cf. Fig.

S5(d). Another major difference between  $p_{x(y)}$  and  $p_z$  waves lies in the amplitude of the ZBCP, with the former obviously smaller than the latter, as is mentioned in the main text.

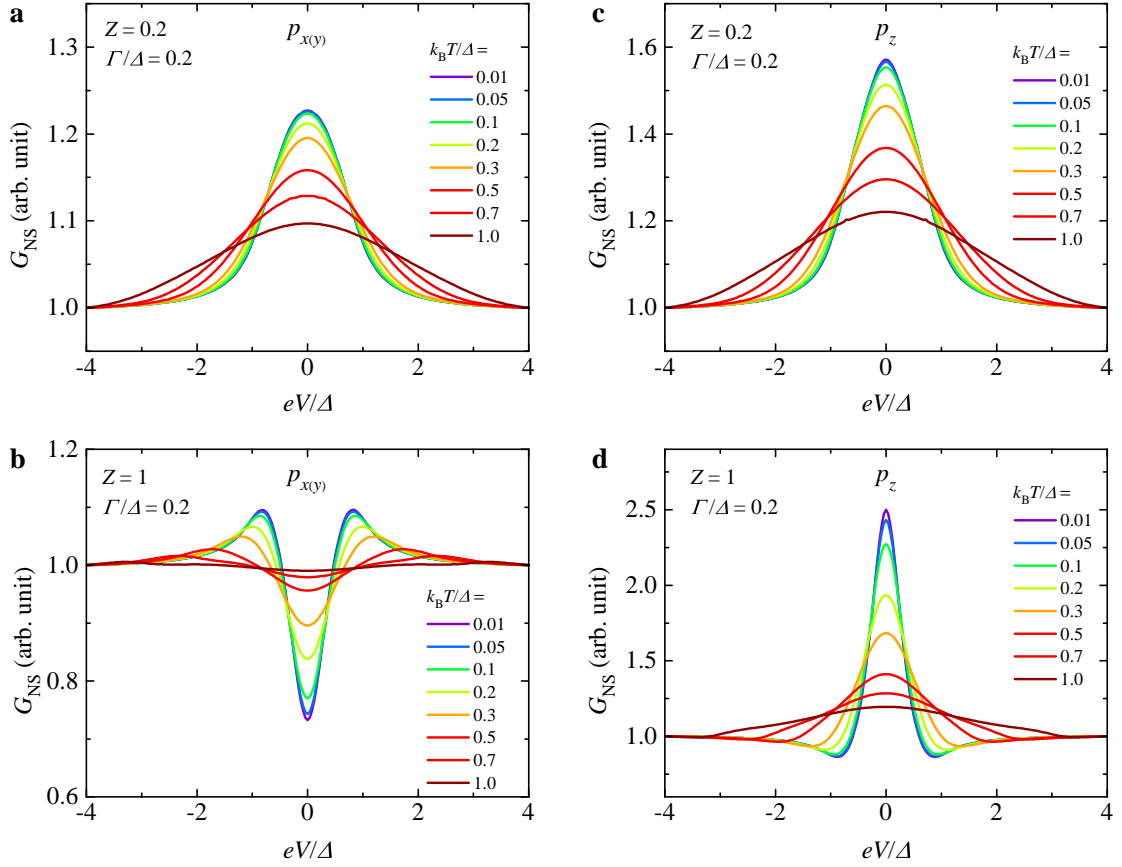


**Figure S5 | Simulated PCS at different temperatures.** The NM-SC junction is on the **x-y** facet. **a**  $p_{x(y)}$ ,  $Z = 0.2$ ,  $\Gamma/\Delta = 0.2$ . **b**  $p_{x(y)}$ ,  $Z = 1$ ,  $\Gamma/\Delta = 0.2$ . **c**  $p_z$ ,  $Z = 0.2$ ,  $\Gamma/\Delta = 0.2$ . **d**  $p_z$ ,  $Z = 1$ ,  $\Gamma/\Delta = 0.2$ . It is found that the behavior of ZBCP with a side-dip is present in  $p_z$ -wave pairing but absent in  $p_{x(y)}$ -wave pairing symmetry.

We then simulate the PCS for different representations, viz  $A_u$ ,  $B_{1u}$ ,  $B_{2u}$  and  $B_{3u}$ , and the results are displayed in Fig. S6. The basis functions of these representations have been listed in Table 1. Note that here we have ignored the high-order ( $k_x k_y k_z$ ) terms. The main parameters used are listed in the figures. For  $A_u$  presentation, a “flattened” ZBCP shows up for  $Z = 0$ , but once  $Z > 0$ , the peak gradually splits into two peaks; a dip appears at  $|V| > 0$  when  $Z > 1$ , as can be seen in Fig. S6(a). For  $B_{1u}$  presentation, a ZBCP is also visible for small  $Z$ , but as  $Z$  increases, it gradually evolves into a zero-bias dip [Fig. S6(b)]. As is shown in Fig. S6(c,d), the ZBCP in the  $B_{2u}$  presentation is robust to the variations of  $Z$  and  $\Gamma$ . In contrast, the finite-bias conductance is highly susceptible. For fixed  $\Gamma = 0.05$

meV, side dips emerge as  $Z$  exceeds 0.8. Furthermore, at  $Z = 1$ , a large  $\Gamma$  of 0.40 meV produces only a shallow, shoulder-like dip. This dip deepens and sharpens into well-defined satellite peaks as  $\Gamma$  is reduced. The  $B_{3u}$  behaves similarly to  $B_{2u}$ . We shall see that  $B_{2u}$  and  $B_{3u}$  capture all the main features of the experimental PCS of UTe<sub>2</sub>.

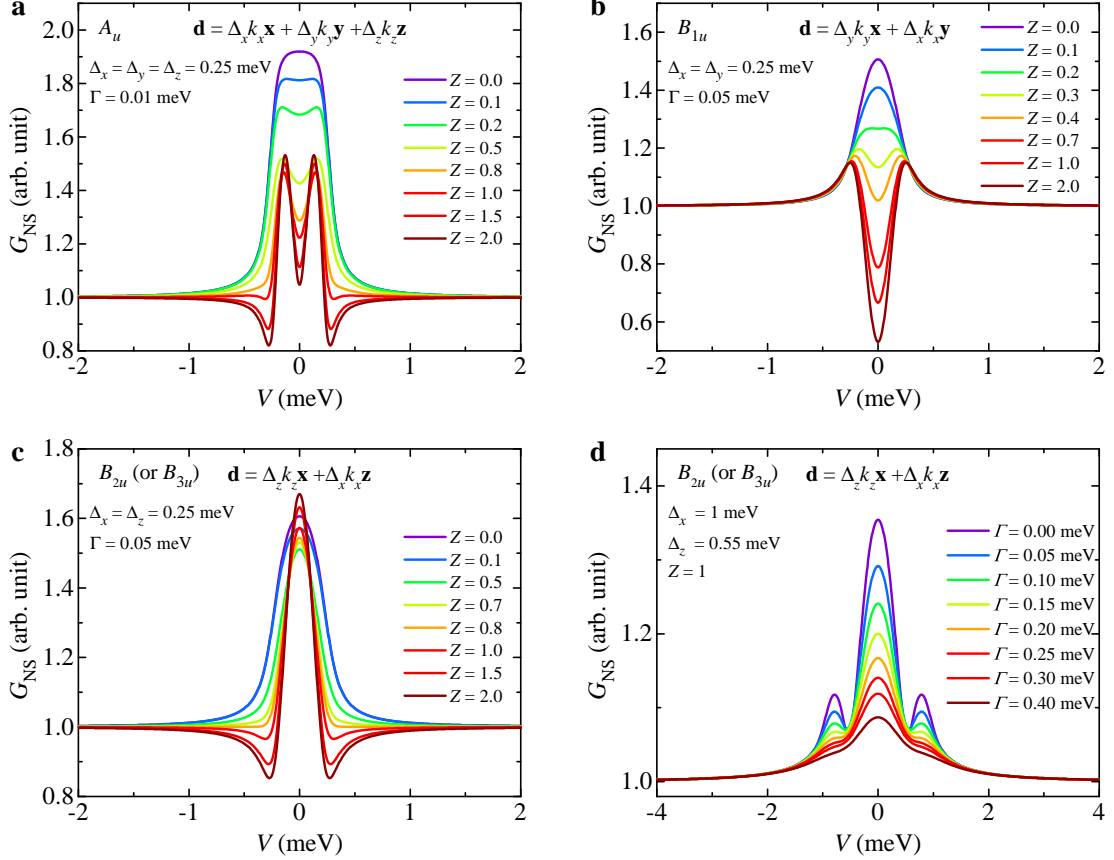
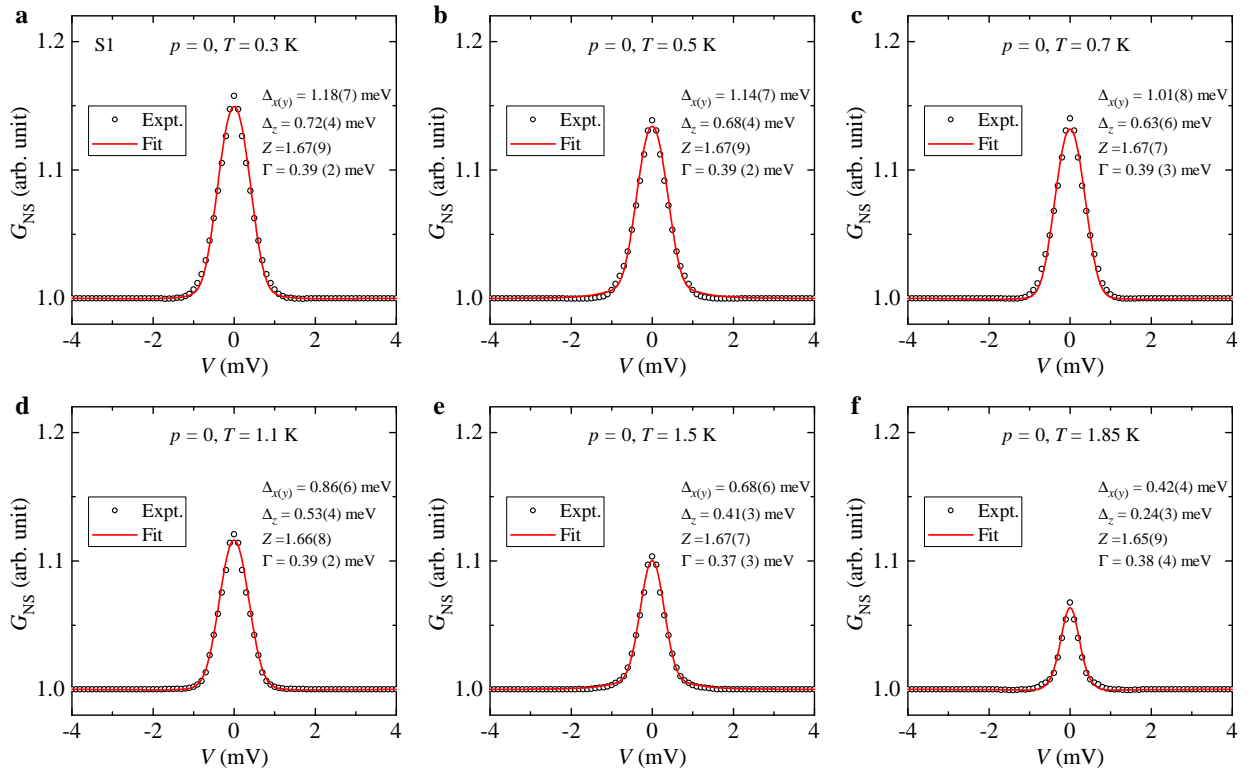


**Figure S6 | Simulated PCS for various irreducible representations.** **a**  $A_u$ . **b**  $B_{1u}$ . **c-d**  $B_{2u}$  or  $B_{3u}$ . Note that for the junction within the  $x$ - $y$  plane, the results of  $B_{2u}$  and  $B_{3u}$  are the same. For  $A_u$ , a zero-bias dip appears for all  $Z > 0$ , and a side dip appears for large  $Z$ . For  $B_{1u}$ , a zero-bias dip appears for large  $Z$ , but no side dip can be obtained. For  $B_{2u}$  and  $B_{3u}$ , the ZBCP persists for all  $Z$ , and a dip on each side appears for large  $Z$ . As  $\Gamma$  decreases, the shoulder may evolves into a satellite peak.

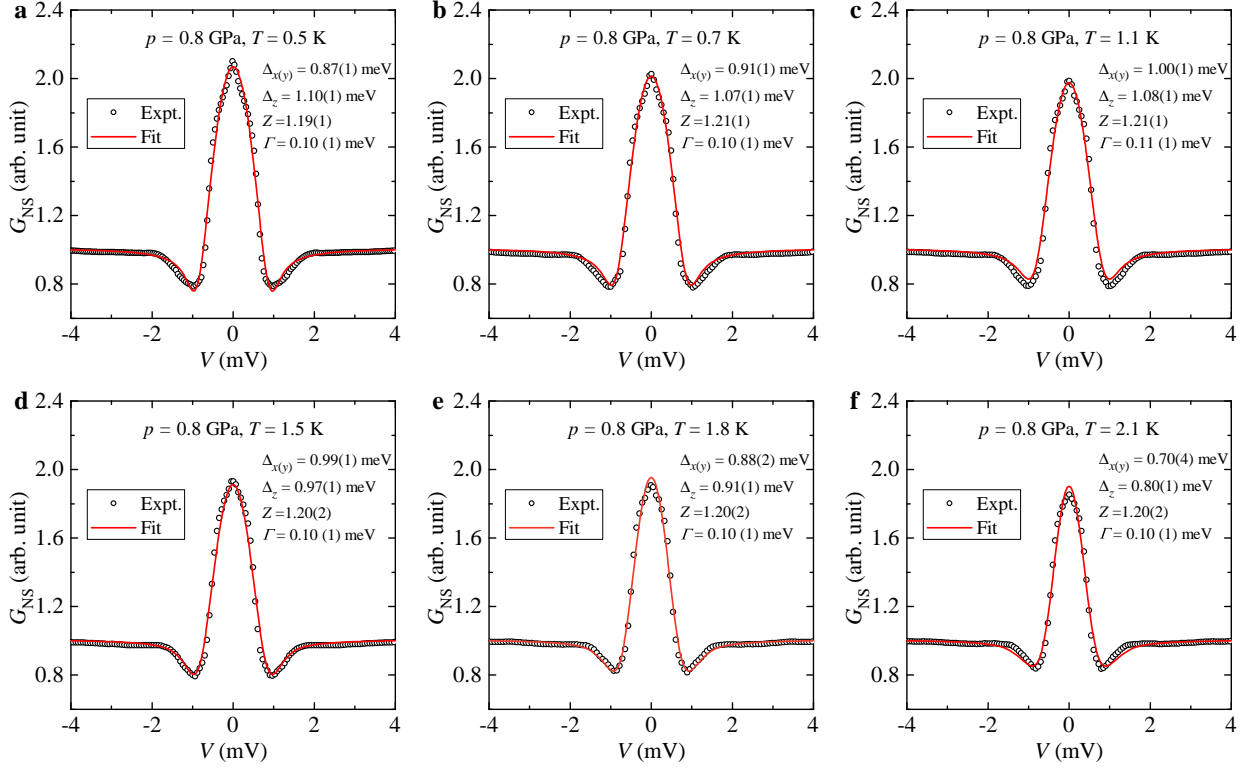
## SI VI: Fitting of the experimental data

TABLE S1: Fitting parameters of PCS at 0.3 K to  $B_{2u}$  (or  $B_{3u}$ ) representation, for samples S1-S3 at  $p = 0$  and  $B = 0$ .

Sample	$\Delta_z$ (meV)	$\Delta_{x(y)}$ (meV)	$Z$	$\Gamma$ (meV)
S1	1.18(7)	0.72(4)	1.67(9)	0.39(2)
S2	1.15(1)	0.62(1)	0.76(1)	0.40(1)
S3	1.15(1)	0.60(1)	1.12(1)	0.16(1)



**Figure S7 | Fitting of the ambient-pressure PCS for sample S1.** **a** 0.3 K. **b** 0.5 K. **c** 0.7 K. **d** 1.1 K. **e** 1.5 K. **f** 1.85 K. The fittings were carried out with  $B_{2u}$  (or  $B_{3u}$ ). The fitting parameters are listed in each panels.



**Figure S8 | Fitting of the point-contact spectra at 0.8 GPa for sample S1. a 0.5 K. b 0.7 K. c 1.1 K. d 1.5 K. e 1.8 K. f 2.1 K.** The fittings were carried out with  $B_{2u}$  (or  $B_{3u}$ ).

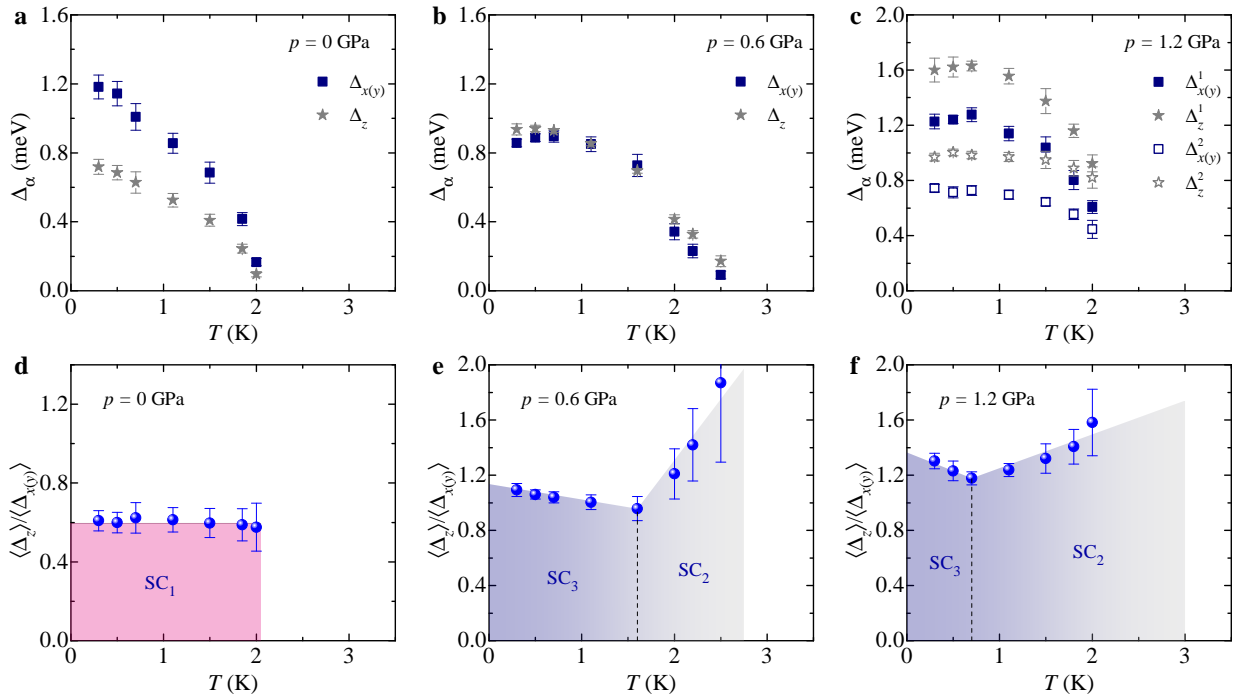


**Figure S9 | The obtained superconducting gap parameters for sample S1. a-c**  $\Delta_\alpha$  [ $\alpha = x(y), z$ ] as a function of temperature for  $p = 0, 0.6$  and  $1.2$  GPa. **d-f**  $\langle \Delta_z \rangle / \langle \Delta_{x(y)} \rangle$ .

---

- [1] Andreev, A. F. Thermal Conductivity of the Intermediate State of Superconductors. *J. Exp. Theor. Phys.* **46**, 1823-1828 (1964).
- [2] Blonder, G. E., Tinkham, M. & Klapwijk, T. M. Transition from metallic to tunneling regimes in superconducting microconstrictions: Excess current, charge imbalance, and supercurrent conversion, *Phys. Rev. B* **25**, 4515-4532 (1982).
- [3] Sigrist, M. & Ueda, K. Phenomenological theory of unconventional superconductivity, *Rev. Mod. Phys.* **63**, 239-311 (1991).
- [4] Setiawan, F. et al. Conductance spectroscopy of topological superconductor wire junctions, *Phys. Rev. B* **91**, 214513 (2015).
- [5] Asano, Y. *Andreev Reflection in Superconducting Junctions* (Springer, 2021).
- [6] Datta, S. *Electronic Transport in Mesoscopic Systems* Ch. 2 (Cambridge Univ. Press, 1995).
- [7] Pleceník, A., Grajcar, M., Beňačka, Š., Seidel, P. & Pfuch, A. Finite-quasiparticle-lifetime effects in the differential conductance of  $\text{Bi}_2\text{Sr}_2\text{CaCu}_2\text{O}_y/\text{Au}$  junctions, *Phys. Rev. B* **49**, 10016-10019 (1994).